Development of East Asia Regional Reanalysis based on advanced hybrid gain data assimilation method and evaluation with E3DVAR, ERA-5, and ERA-Interim reanalysis

Eun-Gyeong Yang, Hyun Mee Kim*, and Dae-Hui Kim

Atmospheric Predictability and Data Assimilation Laboratory

Department of Atmospheric Science, Yonsei University, Seoul, Republic of Korea

Submitted to *Earth System Science Data*

June 28, 2021

Revision submitted on January 7, 2022

* *Corresponding author address*: Hyun Mee Kim, Department of Atmospheric Sciences, Yonsei University, 50 Yonsei-ro, Seodaemun-gu, Seoul, 03722, Republic of Korea.

E-mail: khm@yonsei.ac.kr

ABSTRACT

The East Asia Regional Reanalysis (EARR) system is developed based on the advanced hybrid gain data assimilation method (AdvHG) using Weather Research and Forecasting (WRF) model and conventional observations. Based on EARR, the high-resolution regional reanalysis and reforecast fields are produced with 12 km horizontal resolution over East Asia for 2010–2019. The newly proposed AdvHG is based on the hybrid gain approach, weighting two different analysis for an optimal analysis. The AdvHG is different from the hybrid gain in that 1) E3DVAR is used instead of EnKF, 2) 6 h forecast of ERA5 is used to be more consistent with WRF, and 3) the pre-existing, state-of-the-art reanalysis is used. Thus, the AdvHG can be regarded as an efficient approach to generate regional reanalysis dataset due to cost savings as well as the use of the state-of-the-art reanalysis. The upper air variables of EARR are verified with those of ERA5 for January and July 2017 and the ten-year period of 2010-2019. For upper air variables, ERA5 outperforms EARR over two years, whereas EARR outperforms (shows comparable performance to) ERA-I and E3DVAR for January in 2017 (July in 2017). EARR better represents precipitation than ERA5 for January and July in 2017. Therefore, though the uncertainties of upper air variables of EARR need to be considered when analyzing them, the precipitation of EARR is more accurate than that of ERA5 for both two seasons. The EARR data presented here can be downloaded from https://doi.org/10.7910/DVN/7P8MZT for data on pressure levels and https://doi.org/10.7910/DVN/Q07VRC for precipitation.

1. Introduction

Reanalysis datasets have been widely used in the socio-economical field as well as meteorological and climate research areas all over the world. Most of reanalysis datasets consist of global reanalysis whose spatial and temporal resolutions are relatively coarse (e.g., Schubert et al. 1993; Kalnay et al. 1996; Gibson et al. 1997; Kistler et al. 2001; Kanamitsu et al. 2002; Uppala et al. 2005; Onogi et al. 2007; Bosilovich 2008; Saha et al. 2010; Dee et al. 2011; Rienecker et al. 2011; Bosilovich 2015; Kobayashi et al. 2015; Hersbach et al. 2020). As the importance of regional reanalysis dataset emerged, many operational centers and research institutes around the world have been producing the dataset in their own areas (Mesinger et al. 2006; Renshaw et al. 2013; Borsche et al. 2015; Bromwich et al. 2016; Jermey and Renshaw 2016; Zhang et al. 2017; Bromwich et al. 2018; Fukui et al. 2018; He et al. 2019; Ashrit et al. 2020).

The long-term high-resolution datasets are essential to investigate the past extreme weather events which might be associated with mesoscale features such as heavy rainfall events with high spatial and temporal variability which coarser-resolution model cannot represent. The dynamical downscaling approaches can be a solution for generating high-resolution dataset, but they have some issues with insufficient spin-up (Kayaba et al. 2016). Moreover, Fukui et al. (2018) demonstrated that regional reanalysis over Japan assimilating only the conventional observations had the potential to reproduce precipitation fields better than the dynamical downscaling approaches. Ashrit et al. (2020) also found that the high-resolution regional reanalysis over India showed substantial improvements of regional hydroclimatic features during summer monsoon for the period of 1979-1993 compared to the global reanalysis ERA-Interim (ERA-I, Dee et al. 2011) from ECMWF. Furthermore, He et al. (2019) revealed that the pilot regional reanalysis over the Tibetan Plateau was able to represent more accurate

62 precipitation features as well as atmospheric humidity than the global reanalyses of ECMWF
63 (i.e., ECMWF's fifth-generation reanalysis (ERA5, Hersbach et al. 2020) and ERA-I).

64 As part of this effort, regional reanalysis over East Asia were produced based on the
65 Unified Model for the two-year period of 2013-2014 and it was confirmed that regional
66 reanalysis over East Asia is beneficial (Yang and Kim 2017; Yang and Kim 2019). However,
67 because UM was no longer available for generating regional reanalysis over East Asia, another
68 numerical weather prediction (NWP) model and its data assimilation (DA) method are required.

69 To find the most appropriate and cost-efficient DA method for a regional reanalysis over
70 East Asia, several DA methods were compared. Yang and Kim (2021) demonstrated that the
71 hybrid ensemble-variational data assimilation method (E3DVAR) shows the better
72 performance compared to three-dimensional variational data assimilation (3DVAR) and
73 ensemble Kalman filter (EnKF) over East Asia for January and July in 2016. However, it is
74 essential to confirm if this hybrid method is accurate enough to be used for a regional reanalysis
75 over East Asia. Thus, E3DVAR was compared with the latest and the previous reanalysis data
76 from ECMWF (ERA5 and ERA-I) for (re)analysis and (re)forecast variables and it was found
77 that a performance for a regional reanalysis needs to be further improved.

78 For this reason, a new advanced hybrid gain (AdvHG) data assimilation method, which
79 combines E3DVAR and ERA5 based on WRF model, is newly proposed and investigated in
80 this study. A hybrid gain data assimilation method has been developed as a new kind of hybrid
81 methods (Penny 2014). Based on this method, an advanced data assimilation method is newly
82 developed in this study. Finally, using this newly proposed DA method (AdvHG), East Asia
83 regional reanalysis (EARR) system is developed based on WRF model. EARR datasets have
84 been produced for ten-year period of 2010-2019 and are publicly available
85 (https://dataverse.harvard.edu/dataverse/EARR).

86 To investigate the accuracy and uncertainty of the state-of-the-art AdvHG DA algorithm

developed in this study, analysis and forecast atmospheric variables of E3DVAR, AdvHG, WRF-based ERA-I, and WRF-based ERA5 are evaluated for January and July in 2017, respectively. In addition, reforecast precipitation fields of ERA-I and ERA5 from ECMWF are also verified and compared. In this study, the datasets are evaluated for two-month period (January and July in 2017) or ten-year period (2010-2019) depending on the availability of datasets. The reanalysis and (re)forecast fields of the EARR based on AdvHG and ERA5 are verified for ten-year period (2010-2019). In section 2, the EARR system including model, data assimilation method, and observations are explained. In section 3, the evaluation methods are presented. The verification results of (re)analysis and (re)forecast variables are presented in section 4. Section 4.1 presents evaluation results for wind, temperature, and humidity variables, and section 4.2 presents those for precipitation (re)forecast. Section 5 presents data availability. Lastly, summary and conclusions are presented in section 6.

2. Reanalysis system

2.1. Model

In this study, the Advanced Research Weather Research and Forecasting (WRF, v3.7.1) model is used with 12-km horizontal resolution (540 x 432 grid points) and 50 vertical levels (up to 5 hPa) for East Asia domain shown in Fig. 1. The model settings and physics scheme are summarized in Table 1. Analysis fields are obtained every 6 h (00, 06, 12, and 18 UTC) via assimilation of conventional observations with a 6 h assimilation window, and forecast fields are integrated up to 36 h. The ERA5 reanalysis (Hersbach et al. 2020) is used as the first initial condition before the cycling, and as boundary conditions every 6 h.

2.2. Data assimilation methods

2.2.1. E3DVAR

The E3DVAR method is one of hybrid data assimilation methods, which use a static

111 climatological background error covariance (BEC) and ensemble-based flow-dependent BEC,
112 and couples the EnKF and 3DVAR (Zhang et al. 2013). E3DVAR is based on a cost function
113 of 3DVAR. In E3DVAR, EnKF provides flow-dependent BEC as well as updates perturbations
114 for ensemble members. Following Zhang et al. (2013),

$$J^b = J_s^b + J_e^b = \frac{1}{2}\delta\mathbf{x}^{\mathrm{T}}\left[(1-\beta)\mathbf{B} + \beta\mathbf{P}^f \circ \mathbf{C}\right]^{-1}\delta\mathbf{x} \ , \qquad (1)$$

115 where J_s^b is a traditional cost function based on a static climatological BEC **B** and J_e^b is an
116 additional cost function based on ensemble-based BEC $\mathbf{P}^f$. **C** is a correlation matrix for
117 localization of the ensemble covariance $\mathbf{P}^f$. The weighting coefficient β between static and
118 ensemble-based BEC is set to 0.8 in this study. To account for model error for E3DVAR, multi-
119 physics scheme is applied to 40-member ensembles. Yang and Kim (2021) found that E3DVAR
120 is the most appropriate DA method among 3DVAR, EnKF, and E3DVAR methods over East
121 Asia. More detailed information on E3DVAR implemented in this study can be found in Yang
122 and Kim (2021).

123 *2.2.2. Hybrid gain data assimilation method*

124 In the last decade, the traditional hybrid methods have been widely used for many
125 operational centers and research institutes. Recently, Penny (2014) has proposed a new class
126 of hybrid gain methods combining desirable aspects of both variational and EnKF families of
127 algorithms by weighting analyses from 3DVAR and LETKF for an optimal analysis in the
128 Lorenz 40-component model. Since then, this algorithm has been implemented at ECMWF
129 (Bonavita et al. 2015) and at a hybrid global ocean DA system in National Centers for
130 Environmental Prediction (NCEP) (Penny et al. 2015).

131 The hybrid gain algorithm can be described with the following equations:

$$\mathbf{x}_{Hyb}^a = \alpha\mathbf{x}_{\mathrm{det}}^a + (1-\alpha)\overline{\mathbf{x}^a} \ , \qquad \mathbf{(2)}$$

132 where $\mathrm{x}_{\mathrm{Hyb}}^a$, $\mathrm{x}_{\mathrm{det}}^a$, and $\overline{\mathrm{x}^a}$ denote the hybrid analysis, deterministic analysis, and the ensemble

mean analysis from the ensemble-based assimilation method, and α is a tunable parameter (Penny 2014, Houtekamer and Zhang 2016).

The hybrid gain method is different from traditional hybrid methods, in that a hybrid gain approach linearly combines analysis fields from EnKF and variational DA method to produce a hybrid gain analysis rather than linearly combining respective BECs (Penny 2014). Basically, the hybrid gain method is to hybridize two different Kalman gain matrices of ensemble-based [Eq. (4)] and variational data assimilation system [Eq. (5)] as in Eq. (3).

$$\hat{\mathbf{K}} = \beta_1 \mathbf{K}^f + \beta_2 \mathbf{K}^B + \beta_3 \mathbf{K}^B \mathbf{H} \mathbf{K}^f , \quad (3)$$

where

$$\mathbf{K}^f = \mathbf{P}^f \mathbf{H}^{\mathrm{T}} (\mathbf{H} \mathbf{P}^f \mathbf{H}^{\mathrm{T}} + \mathbf{R})^{-1}, \quad (4)$$

$$\mathbf{K}^B = \mathbf{B} \mathbf{H}^{\mathrm{T}} (\mathbf{H} \mathbf{B} \mathbf{H}^{\mathrm{T}} + \mathbf{R})^{-1}. \quad (5)$$

H is an observation operator mapping the model state vector to observation space and **R** is the observation error covariance matrix. The matrices $\mathbf{P}^f$ and **B** indicate the ensemble-based and the static climatological BEC, respectively. By choosing the specific coefficients (β_1=1, $\beta_2 = \alpha$, $\beta_3 = -\alpha$), it can be written as in Eq. (6) and it can give an algebraically equivalent result with Eq. (2) (Penny 2014).

$$\hat{\mathbf{K}} = \mathbf{K}^f + \alpha \mathbf{K}^B (\mathbf{I} - \mathbf{H} \mathbf{K}^f) . \quad (6)$$

One of advantages of the hybrid gain algorithm with respect to its development is that pre-existing operational systems can be used without significant modification for a hybrid analysis (Penny 2014) and independent parallel development of respective methods is allowed (Houtekamer and Zhang 2016). Furthermore, the hybrid gain approach can be considered as a practical and straightforward method in the foreseeable future to combine advantageous features of both ensemble- and variational-based DA algorithms (Houtekamer and Zhang 2016).

More detailed information on this algorithm can be found in Penny (2014).

2.2.3. Advanced hybrid gain data assimilation method

In this study, based on the hybrid gain approach, an advanced hybrid gain data assimilation method (AdvHG) is newly proposed as follows:

$$\mathrm{X}^{a}_{\mathrm{AdvHG}} = \alpha \mathrm{X}^{f(6h)}_{\mathrm{ERA5}} + (1-\alpha)\overline{\mathrm{X}}^{a}_{\mathrm{E3DVAR}}, \qquad \textbf{(7)}$$

where $\mathrm{X}^{f(6h)}_{\mathrm{ERA5}}$ denotes the 6 h forecast of ERA5 reanalysis based on WRF model and $\overline{\mathrm{X}}^{a}_{\mathrm{E3DVAR}}$ denotes the analysis of E3DVAR (Fig. 2). In Eq. (7), α is a tunable parameter and is assigned to be 0.5 in this study. This advanced hybrid gain approach is different from the hybrid gain approach in that 1) E3DVAR analysis is used instead of EnKF, 2) 6 h forecast of ERA5 is used instead of deterministic analysis from variational DA method, and 3) the pre-existing and state-of-the-art reanalysis data (i.e., ERA5) is simply used instead of producing deterministic analysis by assimilation. The reasons for these different approaches proposed in this study are as follows:

1) E3DVAR is used instead of EnKF because Yang and Kim (2021) confirmed that E3DVAR outperforms EnKF for winter and summer seasons over East Asia.

2) Instead of deterministic analysis, the 6 h forecast of ERA5 based on WRF model is used to make the hybrid analysis more balanced and consistent with WRF model, because ERA5 reanalysis fields are based on its own modeling system with coarser resolution, which is different from that of this study.

3) European Centre for Medium-Range Weather Forecasts (ECMWF) reanalysis (ERA5) is used instead of producing our own analysis fields from a variational DA method. This is a very efficient approach because of the cost savings as well as the use of the high-quality latest reanalysis from ECMWF assimilating all currently available observations with the state-of-the-art and advanced technology.

175 Therefore, the approach proposed in this study is called as “advanced hybrid gain method”
176 (denoted as “AdvHG”).

177 *2.3. Observations*

178 The NCEP PrepBUFR [Prepared or QC’d data in BUFR (Binary Universal Form for the
179 Representation of meteorological data) format] conventional observations (global upper air and
180 surface weather observations, NCEP/NWS/NOAA/U.S.DOC 2008) are used every 6 h (00, 06,
181 12, and 18 UTC) for an assimilation by E3DVAR and AdvHG methods (Fig. 1). The PrepBUFR
182 is the output of the final process for preparing the observations to be assimilated in the different
183 NCEP analyses. For observations, rudimentary multi-platform quality control (QC) and more
184 complex platform-specific QC were conducted (e.g., surface pressure, rawinsonde heights and
185 temperature, wind profiler, aircraft wind and temperature) in NCEP (Keyser 2013).
186 Furthermore, if the innovations (i.e., observation minus background) of some observations are
187 greater than 5 times the observational error, then that observation is rejected during assimilation
188 procedure in this study.

189 The assimilated observations are as follows: the surface observations (SYNOP, METAR,
190 Ship, and Buoy), radiosonde observation (SOUND), upper-wind report (PILOT), wind profiler,
191 aircraft, atmospheric motion vector (AMV) wind from a geostationary satellite (GEOAMV),
192 and Scatterometer oceanic surface winds (Scatwind), and precipitable water vapor from global
193 positioning system (GPSPW). The observation errors depending on each observation platform,
194 variable, and vertical levels are assigned based on the default observation error statistics
195 provided in WRFDA system (Table 2). All observations are spatially thinned by 20 km except
196 for AMV thinned by 200 km as done by Warrick (2015), Cotton et al. (2016), and Shin et al.
197 (2016).

198 To evaluate 6 h accumulated precipitation simulated by E3DVAR, AdvHG, ERA-I, and
199 ERA5 over East Asia, global surface weather observations (NCEP PrepBUFR,

NCEP/NWS/NOAA/U.S.DOC 2008) are used every 6 h (00, 06, 12, and 18 UTC). For an evaluation of the monthly precipitation fields, the world monthly surface station climatology (NCDC/NESDIS/NOAA/U.S.DOC et al. 1981) over 4700 different stations (2600 in more recent years) is used.

2.4.Global reanalysis datasets

To compare EARR generated with other reanalysis datasets, ERA5 (Hersbach et al. 2020) and ERA-I (Dee et al. 2011) reanalysis are chosen. The horizontal resolutions of ERA-I and ERA5 are approximately 79 km (TL255) and 31 km (TL639), respectively. Because ERA5 is based on the operational system in 2016, improvements in model physics, numerics, data assimilation, and additional observations over the last decade are the advantages of ERA5 (Hersbach et al. 2018).

In this study, (re)forecast as well as reanalysis fields need to be verified. Regarding reanalysis and (re)forecast fields of ECMWF, reanalysis fields (i.e., ERA5 and ERA-I) downloaded from ECMWF are evaluated (Figs. 3 and 6). There are two different (re)forecast fields (e.g., ERA5_fromECMWF, WRF-based ERA5) used in this study. WRF-based ERA5 and ERA-I are forecast fields based on WRF model with 12 km horizontal resolution where ERA5 and ERA-I are used as initial conditions, respectively. In contrast, ERA5_fromECMWF and ERA-I_fromECMWF are reforecast fields based on ECMWF model not WRF model, so the reforecast fields of ERA5 and ERA-I are provided and downloaded from ECMWF. These reforecast fields are only used for evaluation of precipitation (Figs. 8 and 9). The (re)analysis and (re)forecast fields and corresponding experiments are explained in Table 3.

3. Evaluation method

3.1. Equitable threat score and Frequency bias index

Based on the contingency table (Table 4), ETS is defined as

$$\mathrm{ETS}=\frac{A-A_r}{A+B+C-A_r}, \text{ where } A_r=\frac{(A+B)(A+C)}{A+B+C+D}. \quad \textbf{(8)}$$

The ETS range is from -1/3 to 1 and the value 1 for ETS is a perfect score. ETS is a more balanced score than Probability of Detection (POD) and False Alarm Ratio (FAR), because it is sensitive to both false alarms and misses (Wilson 2010).

FBI is defined as

$$\mathrm{FBI}=\mathrm{Bias}=\frac{A+B}{A+C}. \quad \textbf{(9)}$$

The FBI indicates whether the model tends to over-forecast (too frequently, FBI>1) or under-forecast (not frequent enough, FBI<1) events with respect to frequency of occurrence.

3.2 Probability of detection and False alarm ratio

Based on the contingency table (Table 4), POD is defined as

$$\mathrm{POD}=\frac{A}{A+C}=\frac{\mathrm{Hits}}{\mathrm{Hits}+\mathrm{Misses}}. \quad \textbf{(10)}$$

The POD range is from 0 to 1. POD is required to be used with FAR, because POD can be artificially improved by systematically over-forecasting the events (Wilson 2010).

FAR is defined as

$$\mathrm{FAR}=\frac{B}{A+B}=\frac{\mathrm{False\ alarms}}{\mathrm{Hits}+\mathrm{False\ alarms}}. \quad \textbf{(11)}$$

The range of FAR is from 0 to 1 and its lower score implies a higher accuracy.

3.3 Brier skill score

Verification of the performance of high-resolution forecast with the traditional verification metrics (e.g., ETS, FBI) can be misleading due to double penalty, particularly for highly variable fields (e.g., precipitation). Therefore, as one of spatial verification approaches that do not require forecast to match point observation spatially, neighborhood (fuzzy) verification method, which assumes that slightly displaced forecast can be acceptable and a local

neighborhood can define the degree of allowable displacement (Ebert 2008; Kim et al. 2015; On et al. 2018), is used in this section. According to Ebert (2008), depending on the matching strategy, neighborhood verifications can be categorized into two frameworks: 'single observation-neighborhood forecast (SO-NF)' where neighborhood forecasts surrounding observations are considered, and 'neighborhood observation-neighborhood forecast (NO-NF)' strategies where not only neighborhood forecasts but also neighborhood observations surrounding observations are considered. Due to the absence of high-resolution gridded precipitation observation data in East Asia, various verification scores widely used as 'neighborhood observation-neighborhood forecast (NO-NF)' strategy are not available in this study. Thus, in this section, Brier skill score as one of 'single observation-neighborhood forecast (SO-NF)' strategy is introduced.

The Brier score (BS) is similar to the mean-squared error (MSE) and is defined as (Wilks 2006):

$$\mathrm{BS}=\frac{1}{N}\sum_{i=1}^{N}(p_i-o_i)^2 . \qquad \textbf{(12)}$$

where p_i denotes the probability forecast, and o_i denotes the binary observation which is either 0 or 1, and N is the total number of observations during the given period. Generally, Brier skill score (or Brier score) is used to verify ensemble forecasts which are able to calculate probabilistic forecasts (Kay et al. 2013; Kim and Kim 2017). However, Brier skill score can also be used for deterministic forecasts using a pragmatic post-processing procedure (Theis et al., 2005; Mittermaier 2014), which derives probabilistic forecasts from deterministic forecasts at every model grid point by considering neighborhood forecast as *pseudo ensemble*.

$$\mathrm{BSS}=1-\frac{\mathrm{BS}}{\mathrm{BS}_{\mathrm{ref}}}, \qquad \textbf{(13)}$$

where $\mathrm{BS}_{\mathrm{ref}}$ is Brier score of reference. Brier skill score is skill score with respect to Brier score

as in Eq. (13). For reference, a climatology or other forecast can be used either. In this study, the WRF-based ERA-I is considered as a reference.

3.4 Pattern correlation coefficient

The pattern correlation coefficient (PCC) is defined as Eq. (14) (Shiferaw et al. 2018; Yoo and Cho 2018; Park and Kim 2020).

$$\mathrm{PCC} = \frac{\sum_{i=1}^{N}(x_i - \bar{x})(o_i - \bar{o})}{\left[\sum_{i=1}^{N}(x_i - \bar{x})^2 \sum_{i=1}^{N}(o_i - \bar{o})^2\right]^{1/2}}, \quad \textbf{(14)}$$

where x_i and o_i are (re)forecast and observed precipitation at ith observation location and the over-bar indicates the averaged variables over N observed stations in the verification area.

4. Results

4.1 Evaluation of wind, temperature, and humidity variables

4.1.1 RMSE for January and July 2017

The analysis and forecast RMSEs of E3DVAR, AdvHG, the WRF-based ERA-I, and WRF-based ERA5 are calculated for zonal wind, meridional wind, temperature, and Qvapor (water vapor mixing ratio in WRF) variables against sonde observations at 00 and 12 UTC in verification domain (dashed box in Fig. 1) for January and July in 2017 and averaged over each month (Figs. 3, 4, and 5).

For analysis RMSE (Fig. 3), E3DVAR is smaller than AdvHG for all pressure levels and variables, except for temperature in July at 1000 hPa and Qvapor in January and July at 1000 hPa. In general, the analysis RMSE of AdvHG for all variables is comparable to or greater than that of ERA5. The analysis RMSE of ERA5 is smaller than that of ERA-I for all levels and variables; in particular, the analysis RMSE difference between ERA5 and ERA-I is distinctive for wind.

Regarding wind variables of analysis (Figs. 3a, b, c, and d), E3DVAR is the most closely fitted to observations except for the wind in upper troposphere in January, followed by ERA5, AdvHG, and ERA-I. For temperature RMSE (Figs. 3e and f), E3DVAR is smaller than AdvHG. For Qvapor, RMSE in July is much larger than that in January due to a monsoonal flow carrying moist air to East Asia. In general, Qvapor RMSE of E3DVAR is the smallest, followed by ERA5, AdvHG, and ERA-I. Therefore, for all variables, generally E3DVAR analysis fields are the most closely fitted to observations. Since the analysis RMSE implies how much analysis fields are fitted to observations rather than the accuracy of analysis itself, not only analysis RMSE but also forecast RMSE should be considered.

For 24 h forecast fields in January (Figs. 4a, c, e, and g), overall, RMSEs of AdvHG and E3DVAR are greater than those of ERA5 and smaller than those of ERA-I, and AdvHG RMSE is smaller than E3DVAR RMSE for all levels and variables. Meanwhile, for July (Figs. 4b, d, f, and h), AdvHG and E3DVAR show comparable RMSE to ERA-I.

Furthermore, general features of 36 h forecast RMSE (Fig. 5) are similar to the 24 h forecast RMSE (Fig. 4). However, particularly in January, the 36 h forecast RMSE differences between ERA5 and ERA-I are more distinctive compared to those of 24 h forecast. In January, the vertically averaged 36 h forecast RMSE differences of ERA5 and ERA-I are 0.52 m s^{-1} for wind, 0.16 K for temperature, and 0.08 g kg^{-1} for Qvapor, whereas those of 24 h forecast are 0.4 m s^{-1} for wind, 0.11 K for temperature, and 0.06 g kg^{-1} for Qvapor. In addition, the 36 h forecast RMSE differences between ERA5 and AdvHG for January are on average 0.1 m s^{-1} for wind, 0.05 K for temperature, and 0.02 g kg^{-1} for Qvapor, which are even smaller compared to those of 24 h forecast, implying that AdvHG is a lot more accurate than ERA-I for January in 2017. For July, 36 h forecast RMSE of ERA5 is the smallest and RMSEs of AdvHG and E3DVAR are similar to those of ERA-I.

4.1.2 RMSE and spread for the period of 2010-2019

309 In this section, EARR produced in this study is verified for a longer period with WRF-
310 based ERA5. RMSE and spread of reanalyses and reforecasts based on AdvHG method are
311 calculated and averaged over the period of 2010-2019. The reanalyses and (re)forecast fields
312 are evaluated by calculating RMSE valid at 00 and 12 UTC and spread at 00, 06, 12, and 18
313 UTC.

314 The averaged RMSEs of reanalysis for ERA5 and EARR (denoted as AdvHG in Fig. 6)
315 and spread of analysis and 6 h forecast fields of EARR (AdvHG) are shown in Fig. 6. With
316 respect to spread, the ensemble spreads of analysis fields are smaller than those of 6 h forecast
317 fields, on average, by 0.15 m s^{-1} for wind, 0.04 K for temperature, and 0.02 g kg^{-1} for Qvapor,
318 which is the well-known characteristics of ensemble-based data assimilation methods. To be
319 specific, the wind spread (Figs. 6a and b) is similar to or greater than the wind RMSE except
320 for the upper troposphere above 200 hPa, implying ensemble spread for wind is well
321 represented below 200 hPa. On the contrary, the ensembles for temperature and Qvapor (Figs.
322 6c and d) are underdispersive compared to their RMSEs.

323 Regarding reanalysis RMSE, overall AdvHG RMSE is greater than ERA5 RMSE for all
324 variables (Fig. 6). The vertically averaged RMSEs of AdvHG are greater by 0.16 m s^{-1} for wind,
325 0.09 K for temperature, and 0.01 g kg^{-1} for Qvapor than those of ERA5. Nonetheless, the wind
326 RMSEs of AdvHG are similar to those of ERA5 for the middle of troposphere (400–850 hPa),
327 and the Qvapor RMSEs of AdvHG are similar to those of ERA5 except for 1000 hPa.

328 In addition, regarding 24 h forecast RMSE, AdvHG shows larger RMSE than ERA5 for
329 all variables (Fig. 7). The vertically-averaged RMSE differences of wind, temperature, and
330 Qvapor variables between AdvHG and ERA5 are approximately 0.2 m s^{-1}, 0.07 K, and 0.03 g
331 kg^{-1}, respectively. These differences are smaller, compared to the 24 h forecast RMSE
332 difference between ERA-I and ERA5 shown in Fig. 4 (i.e., wind, temperature, and Qvapor
333 RMSE difference: 0.4 m s^{-1}, 0.11 K, and 0.06 g kg^{-1} for January 2017, 0.25 m s^{-1}, 0.05 K, and

334 0.04 g kg^{-1} for July 2017).

335 *4.2 Evaluation of precipitation for January and July in 2017.*

336 *4.2.1 Evaluation metrics*

337 *4.2.1.1 Equitable threat score and Frequency bias index*

338 In this section, for the point-based Equitable threat score (ETS) and Frequency bias index
339 (FBI) based on Table 4, the 6 h accumulated precipitation fields based on the 6 h forecast of
340 E3DVAR, AdvHG, WRF-based ERA-I, WRF-based ERA5, ERA-I_fromECMWF, and
341 ERA5_fromECMWF are evaluated every 6 h (00, 06, 12, and 18 UTC) for January and July in
342 2017 (Fig. 8). Here, all the WRF-based precipitation fields are based on 12-km horizontal
343 resolution, and ERA-I_fromECMWF and ERA5_fromECMWF have 79- and 31-km horizontal
344 resolutions, respectively. Generally, ETS decreases as a threshold increases for both two
345 months (Figs. 8a and c). For January in 2017 (Fig. 8a), AdvHG ETS is the greatest among
346 others. Compared to precipitation reforecasts from ECMWF (i.e., ERA-I_fromECMWF,
347 ERA5_fromECMWF), AdvHG shows the higher ETS, indicating that AdvHG is able to
348 simulate more accurate precipitation fields than ERA-I and ERA5 from ECMWF in January
349 2017. Surprisingly, ETS of ERA5_fromECMWF for January in 2017 is the lowest among all
350 the results compared and is even lower than that of ERA-I_fromECMWF.

351 Since the precipitation reforecasts from ECMWF have not only coarser resolutions but
352 also different forecast model (i.e., the forecasting system of ECMWF), the precipitation
353 forecasts of ERA5 and ERA-I are additionally produced by using the same forecast model with
354 the same resolution as AdvHG and E3DVAR in this study, as explained in section 2.4. For
355 January 2017 (Fig. 8a), ETS of ERA5 (i.e., WRF-based ERA5) is higher than that of
356 ERA5_fromECMWF for all thresholds, whereas ETS of ERA-I (i.e., WRF-based ERA-I) is
357 lower than that of ERA-I_fromECMWF except for high thresholds (8 and 16 mm $(6\ h)^{-1}$). The
358 ERA5 ETS is greater than the ERA-I ETS, but is smaller than the AdvHG ETS. The AdvHG

shows the greatest ETS among others with the same resolution and forecast model, and E3DVAR, ERA5, and ERA-I follow.

Regarding FBI in winter (Fig. 8b), for 4, 8, and 16 mm $(6\ h)^{-1}$ thresholds, all the results show the FBI smaller than 1, implying the underestimation of frequency of precipitation for high-threshold events. In general, AdvHG shows the FBI closest to 1 among all the results, which is consistent with the greatest ETS of AdvHG. The E3DVAR FBI is similar to the AdvHG FBI, and ERA5 and ERA-I FBIs are similar to each other.

Meanwhile, overall, the ETS values for January whose maximum is around 0.4 (Fig. 8a) are much greater than those for July in 2017 whose maximum is around 0.2 (Fig. 8c), implying that the precipitation forecast in summer is more difficult than that in winter. The ETS difference between the results in July is smaller than those in January. Particularly, for the thresholds 4 and 8 mm $(6\ h)^{-1}$, ETSs in July are similar to each other (Fig. 8c). Except for those two thresholds, the ETS of ERA-I_fromECMWF is the smallest. At the threshold 16 mm $(6\ h)^{-1}$, ERA5 ETS is the highest, followed by AdvHG, E3DVAR, ERA-I, ERA5_fromECMWF, and ERA-I_fromECMWF. At the threshold 0.5 and 1 mm $(6\ h)^{-1}$, the E3DVAR ETS is the greatest, followed by ERA5, AdvHG, ERA5_fromECMWF, ERA-I, and ERA-I_fromECMWF.

With respect to FBI in July 2017, the WRF-based results show the FBIs greater than 1, whereas reforecast from ECMWF show the FBIs greater than 1 for 0.5, 1, and 4 mm $(6\ h)^{-1}$ thresholds and smaller than 1 for higher thresholds (8 and 16 mm $(6\ h)^{-1}$) (Fig. 8d). For July in 2017, in general, ERA5_fromECMWF FBI is the closest to 1, followed by E3DVAR, AdvHG, ERA5, ERA-I, and ERA-I_fromECMWF FBI.

4.2.1.2 Probability of detection and False alarm ratio

The Probability of Detection (POD or Hit Rate) and False Alarm Ratio (FAR) are calculated for precipitation simulated from E3DVAR, AdvHG, WRF-based ERA-I, WRF-based ERA5, ERA-I_fromECMWF, and ERA5_fromECMWF for January and July in 2017

(Fig. 9). For January in 2017, AdvHG POD is the greatest among the WRF-based results, followed by E3DVAR, ERA5, and ERA-I (Fig. 9a). In addition to the lowest ETS of ERA5_fromECMWF for January in 2017 as discussed in the section 4.2.1.1, FAR of ERA5_fromECMWF is extremely high with low POD in winter. Therefore, especially for January in 2017, the precipitation fields simulated from EARR (AdvHG) over East Asia are a lot more accurate than those from ERA5_fromECMWF.

For July in 2017, generally, AdvHG shows the largest POD, except for ERA5 (Fig. 9c). With respect to FAR, FAR values in July are much greater than those in January, which is consistent with the ETS difference between these two seasons.

4.2.1.3 Brier skill score

The neighborhood sizes are chosen to be $3\Delta x$, $5\Delta x$, $9\Delta x$, and $11\Delta x$, which are 36, 60, 108, and 132 km, respectively, and the thresholds 0.5, 1, 4, 8, and 16 mm $(6\ h)^{-1}$ are considered. The probabilistic precipitation forecasts are calculated at every model grid point depending on neighborhood sizes and thresholds. Regarding each observation, the nearest model grid point to observations is considered as the center of neighborhood. For verification, 6 h accumulated precipitation fields are extracted from the first 0–6 h forecast fields of WRF-based ERA-I, WRF-based ERA5, E3DVAR, and AdvHG every 6 h (00, 06, 12, and 18 UTC). BSSs of ERA5_fromECMWF and ERA-I_fromECMWF are not calculated, because they have different resolution from WRF-based results.

Based on the neighborhood approach, Brier skill score (BSS) is calculated depending on different neighborhood sizes for January and July in 2017, respectively (Fig. 10). Because the reference of Brier score is chosen as the ERA-I, the positive BSS implies better accuracy than ERA-I. In general, for both two months, AdvHG BSS is greater than ERA5 BSS. Although the E3DVAR BSS is the greatest in July 2017, the AdvHG BSS is the greatest in January 2017.

For January in 2017, as a neighborhood size increases, AdvHG and E3DVAR BSSs tend

409 to increase except for ERA5. Overall, AdvHG BSS is the greatest among other BSSs for all
410 thresholds for all neighborhood sizes. The ERA5 BSS is greater than E3DVAR BSS except for
411 16 mm $(6\ h)^{-1}$. The highest BSS of AdvHG and the lowest BSS of ERA-I are consistent with
412 ETS result. Unlike greater E3DVAR ETS than ERA5 ETS, ERA5 BSS is greater than E3DVAR
413 BSS in January 2017.

414 For July 2017, while the ETS difference between the WRF-based results is not distinct
415 (Fig. 8c), the BSS difference is rather noticeable. Generally, E3DVAR BSS is the greatest
416 among other BSSs for all thresholds except for 16 mm $(6\ h)^{-1}$ for neighborhood sizes 9 and 11.
417 Although E3DVAR BSS is the largest, AdvHG outperforms ERA5 and ERA-I. The worst
418 performance of ERA-I precipitation is consistent with ETS result. At 0.5, 1, and 4 mm $(6\ h)^{-1}$
419 thresholds, E3DVAR BSS is the greatest, which is similar to ETS. At 8 and 16 mm $(6\ h)^{-1}$
420 thresholds, ERA5 ETS is the highest, followed by AdvHG and E3DVAR, whereas overall
421 E3DVAR BSS is the highest, followed by AdvHG and ERA5.

422 *4.2.2 Spatial distribution*

423 *4.2.2.1 6 h accumulated precipitation with the pattern correlation coefficient*

424 In this section, the spatial distributions of 6 h accumulated precipitation from the WRF-
425 based forecast and reforecast from ECMWF are compared. In addition, pattern correlation
426 coefficients (PCC) are calculated and shown at the bottom right of Figs. 11 and 12.

427 The PCC is computed according to the usual Pearson correlation operating on the N
428 observed point pairs of 6 h accumulated precipitation fields simulated from (re)forecast and
429 observations at the specific time. For the calculation of PCC, 6 h accumulated precipitation
430 fields from (re)forecast fields are interpolated bilinearly to the N observed points.

431 Firstly, on 29th and 30th of January in 2017 (Fig. 11), it is noticeable that the precipitation
432 fields of AdvHG match observations well over East Asia, whereas, in particular, those of
433 ERA5_fromECMWF do not. For example, ERA5_fromECMWF overestimates precipitation

over inland area of China (Fig. 11zz), while AdvHG simulates precipitation similar to observations regarding its position and intensity (Fig. 11x). ERA5_fromECMWF also shows noticeably smaller PCC (Figs. 11g, n, and zz). Although PCC does not represent the exact accuracy or predictability of precipitation, the overall feature of PCC is consistent with the results found so far. For January in 2017, the averaged PCC of AdvHG is the greatest (i.e., 0.61) and that of ERA5_fromECMWF is the smallest (i.e., 0.46) (not shown).

For 1st and 2nd of July in 2017 (Fig. 12), in general, AdvHG, E3DVAR, and ERA5 well simulate not only overall features of precipitation fields but also their intensity. During July in 2017, ERA5 and ERA-I simulate heavier precipitation than AdvHG (not shown), which is consistent with larger FBI of ERA5 and ERA-I at higher thresholds. For one-month period of July in 2017, the averaged PCC of ERA5 is the greatest (i.e., 0.37) and that of AdvHG is 0.34, but the PCC difference between ERA5 and AdvHG is not distinctive. Moreover, the overall range of averaged PCC of different datasets in summer (i.e., 0.29-0.35) is smaller than that in winter (i.e., 0.46-0.61), which is consistent with the seasonal difference of ETS in this study.

4.2.2.2 Monthly accumulated precipitation

In this section, the monthly accumulated precipitation fields of rain gauge based observations, E3DVAR, AdvHG, ERA-I, ERA5, ERA-I_fromECMWF, and ERA5_fromECMWF are compared to each other for two one-month periods in January and July in 2017, respectively.

The monthly accumulated precipitation fields simulated by E3DVAR and AdvHG (Figs. 13b and c) are similar to each other, and E3DVAR and AdvHG produce the best fit to observed fields. Especially, for the north-western part of Japan (e.g., Chugoku and Kinki), E3DVAR and AdvHG are able to represent precipitation correctly, whereas ERA-I_fromECMWF and ERA5_fromECMWF fail to do so (Fig. 13). Moreover, although all the results similarly represent overall features of precipitation in January (Fig. 13), ERA5_fromECMWF (Fig. 13g)

simulates the overestimated precipitation over South China, which is consistent with the results in the previous section as well as its larger FBI at lower thresholds (0.5 and 1 mm $(6\ h)^{-1}$) shown in Fig. 8b. It is noticeable that all results fail to represent the observed precipitation area over Tibetan Plateau (25°–40°N, 95°–105°E).

For the monthly accumulated precipitation in July 2017, overall, the ERA5_fromECMWF (Fig. 14g) and the WRF-based results (Figs. 14b, c, and e) except for ERA-I (Fig. 14d) well simulate precipitation similar to observations. The WRF-based results including AdvHG overestimate precipitation over western and southern part of Japan, while ERA-I_fromECMWF and ERA5_fromECMWF simulate similar precipitation fields to observed fields. The WRF-based results tend to overestimate precipitation in South China, Korea, and Japan, compared to ERA-I_fromECMWF and ERA5_fromECMWF. This is consistent with the result in Fig. 8d, in which FBIs from WRF-based results are generally greater than for higher thresholds (8 and 16 mm $(6\ h)^{-1}$), whereas those from ECMWF are smaller than 1.

Even though detailed precipitation features of WRF-based results are different, overall features of precipitation from WRF-based results are similar to each other, which implies that predictability of precipitation strongly depends on the physics schemes as well as NWP model, especially for summer season. According to Que et al. (2016), depending on the combinations of physics options in WRF model, the spatial distribution of precipitation can be significantly different over Asian summer monsoon area and YSU PBL scheme which is used in this study tends to overestimate precipitation over the same area. Thus, different physics options could simulate the different spatial distribution of precipitation.

In addition, compared to ERA5 based on WRF model (Fig. 14e), ECMWF model for ERA5_fromECMWF (Fig. 14g) seems to suppress precipitation. Thus, WRF model with the physics schemes used in this study might simulate more precipitation than ECMWF model, although the initial condition is the same. Therefore, it is important to consider the consistency

484 of the systems for data assimilation and forecast model for a good performance of forecast
485 weather variables like precipitation.

486 5. Data Availability

487 The EARR data presented in this study are available every 6 h (i.e., 00, 06, 12, and 18
488 UTC) for the period of 2010-2019 from Harvard Dataverse Repository
489 (https://dataverse.harvard.edu/dataverse/EARR). The EARR 6 hourly data on pressure levels
490 (https://doi.org/10.7910/DVN/7P8MZT, Yang and Kim 2021b) and 6 hourly precipitation data
491 (https://doi.org/10.7910/DVN/Q07VRC, Yang and Kim 2021c) are provided in NetCDF file
492 format.

493 The EARR 6 hourly data on pressure levels (Yang and Kim 2021b) include u-component
494 of wind, v-component of wind, temperature, geopotential height, and specific humidity
495 variables of reanalysis on pressure levels (i.e., 925, 850, 700, 500, 300, 200, 100, and 50 hPa).
496 The EARR 6 hourly precipitation data (Yang and Kim 2021c) contain 6 h accumulated total
497 precipitation variable of 6 h reforecast on single level. The 6 h accumulated total precipitation
498 is obtained from 6 h reforecast field which is integrated for 6 h from reanalysis field every 6 h
499 (i.e., 00, 06, 12 and 18 UTC).

500 6. Summary and conclusions

501 In this study, to develop the regional reanalysis system over East Asia, the advanced
502 hybrid gain algorithm (AdvHG) is newly proposed and evaluated with traditional hybrid DA
503 method (E3DVAR) as well as existing reanalyses from ECMWF (ERA5 and ERA-I) for
504 January and July in 2017. The East Asia Regional Reanalysis (EARR) system is developed
505 based on the AdvHG as the data assimilation method using WRF model and conventional
506 observations. The high-resolution regional reanalysis and reforecast fields over East Asia with
507 12 km horizontal resolution are produced and evaluated against observations with ERA5 for

508 the ten-year period of 2010–2019.

509 The AdvHG newly proposed in this study is based on the hybrid gain approach, weighting
510 analyses from variational-based and ensemble-based DA algorithms to generate optimal hybrid
511 analysis, which can play an important role as a simple and practical method in the foreseeable
512 future to take advantage of each strength of two different DA methods. The advanced hybrid
513 gain method is different from the hybrid gain approach in that 1) E3DVAR is used instead of
514 EnKF, 2) 6 h forecast of ERA5 is used instead of deterministic analysis for a more balanced
515 and consistent analysis with WRF model, and 3) the pre-existing and state-of-the-art reanalysis
516 data (i.e. ERA5) is simply used instead of producing our own analysis fields from a variational
517 DA method. Thus, it can be regarded as an efficient approach to generate regional reanalysis
518 dataset because of cost savings as well as the use of the state-of-the-art reanalysis from
519 ECMWF that assimilates all available observations.

520 For a verification, the latest ECMWF reanalysis and reforecast datasets (i.e., ERA5 and
521 ERA-I) are used. With respect to forecast variables, two different forecast fields of ECWMF
522 are used: 1) reforecast fields from ECMWF (i.e., ERA5_fromECMWF and ERA-
523 I_fromECMWF) and 2) forecast fields (i.e., WRF-based ERA5 and WRF-based ERA-I)
524 integrated in WRF model with 12 km resolution using ERA5 and ERA-I as initial conditions.

525 Analysis and forecast wind, temperature, and humidity variables of AdvHG are evaluated
526 with ERA5 for the ten-year period and evaluated with five different experiments (i.e., E3DVAR,
527 ERA5, ERA-I, ERA5_fromECMWF, ERA-I_fromECMWF) for January and July in 2017.
528 Overall, the analysis RMSE of E3DVAR is the smallest among others but comparable to that
529 of ERA5, especially for January in 2017. Regarding forecast variables, AdvHG outperforms
530 E3DVAR for January and July in 2017. Although ERA5 outperforms AdvHG for upper air
531 variables for two seasons in 2017, AdvHG outperforms ERA-I in January and shows
532 comparable performance to ERA-I in July. Additionally the verification results of AdvHG and

ERA5 for the period of 2010-2019 are consistent with those for two one-month period in 2017.

The precipitation forecast variables are also verified regarding a neighborhood-based verification score (i.e., Brier skill score) as well as the point-based verification scores (i.e., ETS, FBI, POD, and FAR). According to the point-based verification scores, the precipitation forecast of AdvHG in January is the most accurate, followed by E3DVAR, ERA5, ERA-I. For July, overall ETS values of all results are relatively lower compared to those in January, implying the lower predictability in summer season. In addition, the ETS differences between the results are not distinctive in July. For higher thresholds (8 and 16 mm $(6\ h)^{-1}$) in July, AdvHG ETS is greater than E3DVAR ETS and smaller than ERA5 ETS, whereas E3DVAR ETS is the greatest followed by ERA5 and AdvHG for lower thresholds (0.5 and 1 mm $(6\ h)^{-1}$).

To prevent from double penalty when verifying a highly variable data with high resolution (e.g., precipitation), Brier skill score (BSS) based on neighborhood approach is calculated for 6 h accumulated precipitation forecasts depending on different neighborhood sizes for January and July in 2017. In general, BSS of AdvHG is greater than that of ERA5 and ERA-I for both two months. Although the E3DVAR BSS is the greatest in July 2017, the AdvHG BSS is the greatest in January 2017.

Lastly, the spatial distributions of 6 h and monthly accumulated precipitation forecast for AdvHG, E3DVAR, ERA-I, ERA5, ERA-I_fromECMWF, and ERA5_fromECMWF are compared with rain-gauge based observations. For January 2017, it is noticeable that AdvHG precipitation is the closest to observations with highest PCC (i.e., 0.61) and ERA5_fromECMWF overestimates precipitation over South China with the lowest PCC (i.e., 0.46). For July in 2017, the WRF-based results tend to overestimate precipitation compared to ERA-I_fromECMWF and ERA5_fromECMWF. In addition, even though the averaged PCC of ERA5 (i.e., 0.37) is slightly greater than that of AdvHG (i.e., 0.34), the PCC difference

between ERA5 and AdvHG is not distinctive and overall range of averaged PCC of all datasets in summer (i.e., 0.29-0.37) is smaller than that in winter (i.e., 0.46-0.6).

In conclusion, for upper air variables, overall, ERA5 outperforms EARR based on AdvHG, but the RMSE difference between ERA5 and EARR (AdvHG) is smaller than that between ERA5 and ERA-I. In addition, EARR outperforms ERA-I for January 2017 and shows comparable performance to ERA-I for July 2017. On the contrary, according to the evaluation results of precipitation, in general, EARR better represents precipitation than ERA5 as well as ERA5_fromECMWF for January and July in 2017. Even if E3DVAR precipitation is better represented than EARR precipitation for July, the difference is not considerable for July and EARR better simulates precipitation for January than E3DVAR. Therefore, although the uncertainties of upper air variables of EARR should be considered when analyzing them, the precipitation reforecast of EARR is more accurate than that of ERA5 for both two seasons.

Author contribution

Hyun Mee Kim proposed the main scientific ideas and Eun-Gyeong Yang contributed the supplementary ideas during the process. Eun-Gyeong Yang developed the reanalysis system and produced the 10-year regional reanalysis data. Eun-Gyeong Yang and Hyun Mee Kim analyzed the simulation results and completed the manuscript. Dae-Hui Kim contributed to analyzing the reanalysis data and to the preparation of software and computing resources for the reanalysis system.

Competing interests

The authors declare that they have no competing interests.

Acknowledgments

The authors appreciate reviewers for their valuable comments. This study was supported by a National Research Foundation of Korea (NRF) grant funded by the South Korean government (Ministry of Science and ICT) (Grant 2021R1A2C1012572) and the Yonsei Signature Research Cluster Program of 2021 (2021-22-0003). This study was carried out by utilizing the supercomputer system supported by the National Center for Meteorological Supercomputer of Korea Meteorological Administration and Korea Research Environment Open NETwork (KREONET) provided by the Korea Institute of Science and Technology Information. The authors gratefully acknowledge the late Dr. Fuqing Zhang for collaborations at the earlier stages of this study.

References

Ashrit, R., S. Indira Rani, S. Kumar, S. Karunasagar, T. Arulalan, T. Francis, A. Routray, S. I. Laskar, S. Mahmood, P. Jermey, A. Maycock, R. Renshaw, J. P. George, and E. N. Rajagopal, 2020: IMDAA Regional Reanalysis: Performance Evaluation During Indian Summer Monsoon Season. *Journal of Geophysical Research: Atmospheres*, **125**(2), e2019JD030973.

Bonavita, M., M. Hamrud, and L. Isaksen, 2015: EnKF and hybrid gain ensemble data assimilation. Part II: EnKF and hybrid gain results. *Monthly Weather Review*, **143**(12), 4865-4882.

Borsche, M, A. K. Kaiser-Weiss, P. Undén, and F. Kaspar, 2015: Methodologies to characterize uncertainties in regional reanalyses. *Adv. Sci. Res.*, **12**, 207-218.

Bosilovich, M., 2008: NASA's modern era retrospective-analysis for research and applications: Integrating Earth observations. Earthzine, 26 September 2008. [Available online at www.earthzine.org/2008/09/26/nasas-modern-era-retrospective-analysis/.]

Bosilovich, M., R. Lucchesi, and M. Suarez, 2015: MERRA-2: File specification. NASA GMAO Office Note 9, 73 pp., http://gmao.gsfc.nasa.gov/pubs/docs/Bosilovich785.pdf.

Bromwich, D. H., A. B. Wilson, L. Bai, Z. Liu, M. Barlage, C. F. Shih, S. Maldonado, K. M. Hines, S.-H. Wang, J. Woollen, B. Kuo, H.-C. Lin, T.-K. Wee, M. C. Serreze, and J. E. Walsh, 2018: The Arctic system reanalysis, version 2. *Bulletin of the American Meteorological Society*, **99**(4), 805-828.

Bromwich, D. H., A. B. Wilson, L. S. Bai, G. W. Moore, and P. Bauer, 2016: A comparison of the regional Arctic System Reanalysis and the global ERA-Interim Reanalysis for the Arctic. *Quarterly Journal of the Royal Meteorological Society*, **142**(695), 644-658.

Cotton, J., M. Forsythe, F. Warrick, K. Salonen, N. Bormann, and K. Lean, 2016: AMVs in the Tropics: use in NWP, data quality and impact, Joint ECMWF/ESA Workshop on 'Tropical modeling, observations and data assimilation [Available online at https://www.ecmwf.int/node/16865]

Dee, D. P., S. M. Uppala, A. J. Simmons, P. Berrisford, P. Poli, S. Kobayashi, U. Andrae, M. A. Balmaseda, G. Balsamo, P. Bauer, P. Bechtold, A. C. M. Beljaars, L. van de Berg, J. Bidlot, N. Bormann, C. Delsol, R. Dragani, M. Fuentes, A. J. Geer, L. Haimberger, S. B. Healy, H.

621 Hersbach, E. V. Hólm, L. Isaksen, P. Kållberg, M. Köhler, M. Matricardi, A. P. McNally, B. M.
622 Monge-Sanz, J.-J. Morcrette, B.-K. Park, C. Peubey, P. de Rosnay, C. Tavolato, J.-N. Thépaut,
623 and F. Vitart, 2011: The ERA-Interim reanalysis: configuration and performance of the data
624 assimilation system. *Q. J. R. Meteorol. Soc*., **137**, 553–597. doi: 10.1002/qj.828
625 Ebert, E. E., 2008: Fuzzy verification of high-resolution gridded forecasts: a review and proposed
626 framework. *Meteorological Applications: A journal of forecasting, practical applications,*
627 *training techniques and modelling*, **15**(1), 51-64.
628 Fukui, S., T. Iwasaki, K. Saito, H. Seko, and M. Kunii, 2018: A feasibility study on the high-resolution
629 regional reanalysis over Japan assimilating only conventional observations as an alternative to
630 the dynamical downscaling. *Journal of the Meteorological Society of Japan*. **96**(6), 565-585.
631 Gibson, J. K., P. Kållberg, S. Uppala, A. Nomura, A. Hernandez, E. Serrano, 1997: ERA Description.
632 *ECMWF Re-Analysis Final Report Series*, **1**, 71pp.
633 Grell, G. A., and S. R. Freitas, 2014: A scale and aerosol aware stochastic convective parameterization
634 for weather and air quality modeling. *Atmos. Chem. Phys*, **14**(10), 5233-5250.
635 He, J., F. Zhang, X. Chen, X. Bao, D. Chen, H. M. Kim, H.-W. Lai, L. R. Leung, X. Ma, Z. Meng, T.
636 Ou, Z. Xiao, E.-G. Yang, and K. Yang, 2019: Development and evaluation of an ensemble-based
637 data assimilation system for regional reanalysis over the Tibetan Plateau and surrounging
638 regions, *Journal of Advances in Modeling Earth Systems*, **11**(8), 2503-2522.
639 Hersbach, H., B. Bell, P. Berrisford, S. Hirahara, A. Horányi, J. Muñoz-Sabater, J. Nicolas, C. Peubey,
640 R. Radu, D. Schepers, A. Simmons, C. Soci, S. Abdalla, X. Abellan, G. Balsamo, P. Bechtold,
641 G. Biavati, J. Bidlot, M. Bonavita, G. D. Chiara. P. Dahlgren, D. Dee, M. Diamantakis, R.
642 Dragani, J. Flemming, R. Forbes, M. Fuentes, A. Geer, L. Haimberger, S. Healy, R. J. Hogan, E.
643 Hólm, M. Janisková, S. Keeley, P. Laloyaux, P. Lopez, C. Lupu, G. Radnoti, P. de Rosnay, I.
644 Rozum, F. Vamborg, S. Villaume, and J.-N. Thépaut, 2020: The ERA5 global reanalysis.
645 *Quarterly Journal of the Royal Meteorological Society*, **146**(730), 1999-2049.
646 Hersbach, H., P. de Rosnay, B. Bell, D. Schepers, A. Simmons, C. Soci, S. Abdalla, M. Alonso
647 Balmaseda, G. Balsamo, P. Bechtold, P. Berrisford, J. Bidlot, Eric. de Boisséson, M. Bonavita,

P. Browne, R. Buizza, P. Dahlgren, D. Dee, R. Dragani, M. Diamantakis, J. Flemming, R. Forbes, A. Geer, T. Haiden, E. Hólm, L. Haimberger, R. Hogan, A. Horányi, M. Janisková, P. Laloyaux, P. Lopez, J. Muñoz-Sabater, C. Peubey, R. Radu, D. Richardson, J.-N. Thépaut, F. Vitart, X. Yang, E. Zsótér, and H. Zuo, 2018: Operational global reanalysis: progress, future directions and synergies with NWP, *ECMWF ERA report series*, N27.

Hong, S.-Y., Y. Noh, and J. Dudhia, 2006: A new vertical diffusion package with an explicit treatment of entrainment processes. *Monthly Weather Review*, **134**(9), 2318-2341.

Houtekamer, P. L., and F. Zhang, 2016: Review of the ensemble Kalman filter for atmospheric data assimilation. *Monthly Weather Review*, **144**(12), 4489-4532.

Iacono, M. J., J. S. Delamere, E. J. Mlawer, M. W. Shephard, S. A. Clough, and W. D. Collins, 2008: Radiative forcing by long-lived greenhouse gases: Calculations with the AER radiative transfer models. *Journal of Geophysical Research: Atmospheres*, **113**(D13).

Jermey, P. M., and R. J. Renshaw, 2016: Precipitation representation over a two-year period in regional reanalysis. *Q. J. R. Meteorol. Soc.*, **142**, 1300-1310.

Jiménez, P. A., J. Dudhia, J. F. González-Rouco, J. Navarro, J. P. Montávez, and E. García-Bustamante, 2012: A revised scheme for the WRF surface layer formulation. *Mon. Wea. Rev.*, **140**(3), 898-918.

Kayaba, N., T. Yamada, S. Hayashi, K. Onogi, S. Kobayashi, K. Yoshimoto, K. Kamiguchi, and K. Yamashita, 2016: Dynamical regional downscaling using the JRA-55 reanalysis (DSJRA-55). *Sola*, **12**, pp.1-5.

Kalnay, E., M. Kanamitsu, R. Kistler,W. Collins, D. Deaven, L. Gandin, M. Iredell, S. Saha, G. White, J.Woolen, Y. Zhu, M. Chelliah, W. Ebisuzaki, W. Higgins, J. Janowiak, K. C. Mo, C. Ropelewski, J. Wang, A. Leetmaa, R. Reynolds, Roy Jenne and Dennis Joseph, 1996: The NCEP/NCAR 40-year reanalysis project. *Bull. Amer. Meteorol. Soc.*, **77**, 437-471.

Kanamitsu, M., W. Ebisuzaki, J. Woollen, S.-K. Yang, J. J. Hnilo, M. Fiorino, and G. L. Potter, 2002: NCEP–DOE AMIP-II Reanalysis (R-2). *Bull. Amer. Meteor. Soc.*, **83**, 1631–1643.

Kay, J. K., H. M. Kim, Y.-Y. Park, and J. Son, 2013: Effect of doubling ensemble size on the

675 performance of ensemble prediction in warm season using MOGREPS implemented in
676 KMA, *Advances in Atmospheric Sciences,* **30**(5), 1287-1302, doi:10.1007/s00376-012-2083-y.
677 Keyser, D., 2013: An Overview of Observational Data Processing at NCEP (with information on BUFR
678 Format including "PrepBUFR" files), *GSI tutorial*, August 6, 2013.
679 Kim, S., H. M. Kim, J. K. Kay, and S.-W. Lee, 2015: Development and evaluation of high resolution
680 limited area ensemble prediction system in KMA, Atmosphere, 25(1), 67-83. (in Korean with
681 English abstract)
682 Kim, S., and H. M. Kim, 2017: Effect of considering sub-grid scale uncertainties on the forecasts of a
683 high-resolution limited area ensemble prediction system, *Pure and Applied Geophysics*, **174**(5),
684 2021-2037, doi: 10.1007/s00024-017-1513-2.
685 Kistler, R., W. Collins, S. Saha, G. White, J. Woollen, E. Kalnay, M. Chelliah, W. Ebisuzaki, M.
686 Kanamitsu, V. Kousky, H. v. d. Dool, R. Jenne, and M. Fiorino, 2001: The NCEP–NCAR 50–
687 Year Reanalysis: Monthly Means CD–ROM and Documentation. *Bull. Amer. Meteor. Soc.*, **82**,
688 247–267.
689 Kobayashi, S., Y. Ota, Y. Harada, A. Ebita, M. Moriya, H. Onoda, K. Onogi, H. Kamahori, C. Kobayashi,
690 H. Endo, K. Miyaoka, and K. Takahashi, 2015: The JRA-55 reanalysis: General specifications
691 and basic characteristics, *J. Meteorol. Soc. Jpn.*, **93**, 5-48.
692 Mesinger, F., G. DiMego, E. Kalnay, K. Mitchell, P. C. Shafran, W. Ebisuzaki, D. Jović, J. Woollen, E.
693 Rogers, E. H. Berbery, M. B. Ek, Y. Fan, R. Grumbine, W. Higgins, H. Li, Y. Lin, G. Manikin,
694 D. Parrish, and W. Shi, 2006: North American Regional Reanalysis. *Bull. Amer. Meteor. Soc.*,
695 **87**, 343–360.
696 Mittermaier, M. P., 2014: A strategy for verifying near-convection-resolving model forecasts at
697 observing sites. *Weather and Forecasting*, **29**(2), 185-204.
698 National Centers for Environmental Prediction/National Weather Service/NOAA/U.S. Department of
699 Commerce, 2008: NCEP ADP Global Upper Air and Surface Weather Observations
700 (PREPBUFR format). *Research Data Archive at the National Center for Atmospheric Research,*
701 *Computational and Information Systems Laboratory*, Boulder, CO. [Available online at

https://doi.org/10.5065/Z83F-N512.] Accessed 5 July 2018.

National Climatic Data Center/NESDIS/NOAA/U.S. Department of Commerce, Meteorology Department/Florida State University, Climate Analysis Section/Climate and Global Dynamics Division/National Center for Atmospheric Research/University Corporation for Atmospheric Research, and Harvard College Observatory/Harvard University, 1981: World Monthly Surface Station Climatology. *Research Data Archive at the National Center for Atmospheric Research, Computational and Information Systems Laboratory*, Boulder, CO. [Available online at http://rda.ucar.edu/datasets/ds570.0/.] Accessed 7 Nov 2019.

On, N., H. M. Kim, and S. Kim, 2018: Effects of resolution, cumulus parameterization scheme, and probability forecasting on precipitation forecasts in a high-resolution limited-area ensemble prediction system, Asia-Pacific Journal of Atmospheric Sciences, 54, 623-637, doi:10.1007/s13143-018-0081-4.

Onogi, K., J. Tsutsui, H. Koide, M. Sakamoto, S. Kobayashi, H. Hatsushika, T. Matsumoto, N. Yamazaki, H. Kamahori, K. Takahashi, S. Kadokura, K. Wada, K. Kato, R. Oyama, T. Ose, N. Mannoji, and R. Taira, 2007: The JRA-25 reanalysis. *J. Meteor. Soc. Japan,* **85**, 369−432.

Park, J., and H. M. Kim, 2020: Design and evaluation of CO_2 observation network to optimize surface CO_2 fluxes in Asia using observation system simulation experiments, *Atmospheric Chemistry and Physics*, **20**, 5175-5195, https://doi.org/10.5194/acp-20-5175-2020.

Penny, S. G., 2014: The hybrid local ensemble transform Kalman filter. *Monthly Weather Review*, **142**(6), 2139-2149.

Penny, S. G., D. W. Behringer, J. A. Carton, and E. Kalnay, 2015: A hybrid global ocean data assimilation system at NCEP. *Monthly Weather Review*, **143**(11), 4660-4677.

Que, L. J., W. L. Que, and J. M. Feng, 2016: Intercomparison of different physics schemes in the WRF model over the Asian summer monsoon region. *Atmospheric and Oceanic Science Letters*, **9**(3), 169-177.

728 Renshaw, R., P. Jermey, D. Barker, A. Maycock, and S. Oxley, 2013: EURO4M regional reanalysis
729 system, *Forecasting Research Technical Report*, No. **583**, Met Office.
730 Rienecker, M. M., M. J. Suarez, R. Gelaro, R. Todling, J. Bacmeister, E. Liu, M. G. Bosilovich, S. D.
731 Schubert, L. Takacs, G.-K. Kim, S. Bloom, J. Chen, D. Collins, A. Conaty, A. da Silva, W. Gu,
732 J. Joiner, R. D. Koster, R. Lucchesi, A. Molod, T. Owens, S. Pawson, P. Pegion, C. R. Redder,
733 R. Reichle, F. R. Robertson, A. G. Ruddick, M. Sienkiewicz, and J. Woollen, 2011: MERRA:
734 NASA's Modern-Era Retrospective Analysis for Research and Applications. *J. Climate*, **24**,
735 3624–3648.
736 Saha, S., S. Moorthi, H.-L. Pan, X. Wu, J. Wang, S. Nadiga, P. Tripp, R. Kistler, J. Woollen, D. Behringer,
737 H. Liu, D. Stokes, R. Grumbine, G. Gayno, J. Wang, Y.-T. Hou, H.-Y. Chuang, H.-M. H. Juang,
738 J. Sela, M. Iredell, R. Treadon, D. Kleist, P. V. Delst, D. Keyser, J. Derber, M. Ek, J. Meng, H.
739 Wei, R. Yang, S. Lord, H. V. D. Dool, A. Kumar, W. Wang, C. Long, M. Chelliah, Y. Xue, B.
740 Huang, J.-K. Schemm, W. Ebisuzaki, R. Lin, P. Xie, M. Chen, S. Zhou, W. Higgins, C.-Z. Zou,
741 Q. Liu, Y. Chen, Y. Han, L. Cucurull, R. W. Reynolds, G. Rutledge, and M. Goldberg, 2010: The
742 NCEP Climate Forecast System Reanalysis. *Bull. Amer. Meteor. Soc.*, **91**, 1015–1057.
743 Schubert, S., J. Pfaendtner, and R. Rood, 1993: An assimilated dataset for earth science applications.
744 *Bull. Amer. Meteor. Soc.*, **74**, 2331–2342.
745 Shiferaw, A., T. Tadesse, C. Rowe, and R. Oglesby, 2018: Precipitation extremes in dynamically
746 downscaled climate scenarios over the greater horn of Africa. *Atmosphere*, **9**(3), 112.
747 Shin, I.-C, J.-G. Kim, C.-Y. Chung, S.-K. Baek, and J.-R. Lee, 2016: The impact of the COMS data on
748 the KMA NWP System, *14th JCSDA Technical Review Meeting & Science Workshop on*
749 *Satellite Data Assimilation*.
750 Skamarock, W. C., J. B. Klemp, J. Dudhia, D. O. Gill, D. M. Barker, M. G. Duda, X.-Y. Huang, W.
751 Wang, J. G. Powers, 2008: A description of the advanced research WRF version 3. NCAR Tech.
752 Note NCAR/TN-475+ STR Available at:
753 https://opensky.ucar.edu/islandora/object/technotes%3A500/datastream/PDF/view.
754 Tewari, M., F. Chen, W. Wang, J. Dudhia, M. A. LeMone, K. Mitchell, M. Ek, G. Gayno, J. Wegiel, and

R. H. Cuenca, 2004: Implementation and verification of the unified NOAH land surface model in the WRF model. *20th conference on weather analysis and forecasting/16th conference on numerical weather prediction* (Vol. 1115). Seattle, WA: American Meteorological Society.

Theis, S. E., A. Hense, and U. Damrath, 2005: Probabilistic precipitation forecasts from a deterministic model: A pragmatic approach. *Meteorological Applications: A journal of forecasting, practical applications, training techniques and modelling*, **12**(3), 257-268.

Thompson, G., P. R. Field, R. M. Rasmussen, and W. D. Hall, 2008: Explicit forecasts of winter precipitation using an improved bulk microphysics scheme. Part II: Implementation of a new snow parameterization. *Mon. Wea. Rev.*, **136**(12), 5095-5115.

Uppala, S. M., P. W. KÅllberg, A. J. Simmons, U. Andrae, V. D. C. Bechtold, M. Fiorino, J. K. Gibson, J. Haseler, A. Hernandez, G. A. Kelly, X. Li, K. Onogi, S. Saarinen, N. Sokka, R. P. Allan, E. Andersson, K. Arpe, M. A. Balmaseda, A. C. M. Beljaars, L. V. D. Berg, J. Bidlot, N. Bormann, S. Caires, F. Chevallier, A. Dethof, M. Dragosavac, M. Fisher, M. Fuentes, S. Hagemann, E. Hólm, B. J. Hoskins, L. Isaksen, P. A. E. M. Janssen, R. Jenne, A. P. Mcnally, J.-F. Mahfouf, J.-J. Morcrette, N. A. Rayner, R. W. Saunders, P. Simon, A. Sterl, K. E. Trenberth, A. Untch, D. Vasiljevic, P. Viterbo, and J. Woollen, 2005: The ERA-40 re-analysis. *Q. J. R. Meteorol. Soc.*, **131**: 2961–3012.

Warrick, F., 2015: Options for filling the LEO-GEO AMV Coverage Gap. *NWP SAF Tech. Doc.*, NWP SAF-MO-TR-030, 21 p.

Wilks, D. S., 2006: Statistical methods in the atmospheric sciences, 2nd edn., *Academic Press*, 627pp.

Wilson, L., 2010: Verification of severe weather forecasts in support of the ‘‘SWFDP Southern Africa’’ project. *Report for the World Meteorological Organisation*, pp. 21 (www.wmo.int/pages/prog/www/BAS/documents/Doc-7-Verification.doc)

Yang, E.-G., and H. M. Kim, 2017: Evaluation of a regional reanalysis and ERA-Interim over East Asia using in situ observations during 2013-14, *Journal of Applied Meteorology and Climatology*, **56**(10), 2821-2844,

Yang, E.-G., and H. M. Kim, 2019: Evaluation of Short-Range Precipitation Reforecasts from East Asia

Regional Reanalysis. *Journal of Hydrometeorology*, **20**(2), 319-337.

Yang, E.-G., and H. M. Kim, 2021a: A comparison of variational, ensemble-based, and hybrid data assimilation methods over East Asia for two one-month periods, *Atmospheric Research*, **249**, 105257.

Yang, E.-G., and H. M. Kim, 2021b: East Asia Regional Reanalysis 6 hourly data on pressure levels from 2010 to 2019, https://doi.org/10.7910/DVN/7P8MZT, Harvard Dataverse, V1.

Yang, E.-G., and H. M. Kim, 2021c: East Asia Regional Reanalysis 6 hourly precipitation data from 2010 to 2019, https://doi.org/10.7910/DVN/Q07VRC, Harvard Dataverse, V1.

Yoo, C., and E. Cho, 2018: Comparison of GCM precipitation predictions with their RMSEs and pattern correlation coefficients. *Water*, **10**(1), 28.

Zhang, F., M. Zhang, and J. Poterjoy, 2013: E3DVar: Coupling an ensemble Kalman filter with three-dimensional variational data assimilation in a limited-area weather prediction model and comparison to E4DVar. *Monthly Weather Review*, **141**(3), 900-917.

Zhang, Q., Y. Pan, S. Wang, J. Xu, and J. Tang, 2017: High-resolution regional reanalysis in China: Evaluation of 1 year period experiments. *Journal of Geophysical Research: Atmospheres*, **122**(20), 10-801.

Table caption

Table 1. Model configuration.

Table 2. Summary of observations used in this study. The default observation error statistics provided in WRFDA system are used for assimilation in this study. The variables u, v, T, RH, Ps, and TPW denote zonal wind, meridional wind, temperature, relative humidity, surface pressure, and total precipitable water, respectively.

Table 3. (Re)analyses and (re)forecasts and corresponding experiments used in this study.

Table 4. The 2×2 contingency table for dichotomous (yes-no) events.

Figure caption

Figure 1. The East Asia Regional Reanalysis domain with different types of NCEP PrepBUFR observations available for assimilation at 00 UTC on 1st of January in 2017. The black dashed box denotes a verification area.

Figure 2. The schematic diagram of the advanced hybrid gain data assimilation method in the East Asia regional reanalysis system.

Figure 3. RMSEs of analysis of (a,b) zonal wind, (c,d) meridional wind, (e,f) temperature, and (g,h) Qvapor (water vapor mixing ratio) from ERA-I (black dashed), ERA5 (black solid), E3DVAR (blue dashed), AdvHG (blue solid) depending on pressure levels for (left) January and (right) July in 2017.

Figure 4. Same as Fig. 3 except for 24 h forecast.

Figure 5. Same as Fig. 3 except for 36 h forecast.

Figure 6. RMSEs of analysis of (a) zonal wind, (b) meridional wind, (c) temperature, and (d) Qvapor (water vapor mixing ratio) from ERA5 (black solid) and AdvHG (blue solid) and spreads of analysis (black dashed) and 6 h forecast (gray dashed) of AdvHG depending on pressure levels averaged over the ten-year period of 2010-2019.

Figure 7. Same as Fig. 6 except for RMSE of 24 h forecast.

Figure 8. (a,c) ETS and (b,d) FBI for (a,b) January and (c,d) July in 2017 depending on thresholds 0.5, 1, 4, 8, and 16 mm $(6\ h)^{-1}$.

Figure 9. (a,c) POD and (b,d) FAR for (a,b) January and (c,d) July in 2017 depending on thresholds 0.5, 1, 4, 8, and 16 mm $(6\ h)^{-1}$.

Figure 10. Brier skill score of the probabilistic postprocessed forecast with reference to the

WRF-based ERA-I for (a-d) January and (e-h) July in 2017 (Blue solid: AdvHG, blue dashed: E3DVAR, red solid: WRF-based ERA5).

Figure 11. The spatial distribution of 6 h accumulated precipitation of (1st column) observation, (2nd column) E3DVAR, (3rd column) AdvHG, (4th column) ERA-I, (5th column) ERA5, (6th column) ERA-I_fromECMWF, and (7th column) ERA5_fromECMWF and the pattern correlation coefficient (PCC) shown at the bottom right of each figure at valid time (1st low, 3rd low) 06 UTC and (2nd low, 4th low) 18 UTC on 29th and 30th of January in 2017.

Figure 12. As in Fig. 11, but for 1st and 2nd of July in 2017.

Figure 13. The spatial distribution of the monthly accumulated precipitation of (a) observations, (b) E3DVAR, (c) AdvHG, (d) ERA-I, (e) ERA5, (f) ERA-I from ECMWF, and (g) ERA5 from ECMWF for January 2017.

Figure 14. As in Fig. 13, but for July 2017.

843 Table 1. Model configuration

	Description
Hori. Resol.	12 km (540×432 grid points)
Vert. Lev.	50 vertical levels (up to 5 hPa)
Model	WRF Model (v3.7.1, Skamarock et al. 2008)
LBC	ERA5 (Hersbach et al. 2020)
Data assimilation	E3DVAR (Zhang et al. 2013), Adanced hybrid gain method
Microphysics	Thompson scheme (Thompson et al. 2008)
Cumulus convection	Grell–Freitas ensemble scheme (Grell and Freitas 2014)
PBL	Yonsei University scheme (Hong et al. 2006)
Radiation	Rapid Radiative Transfer Model (RRTMG) scheme (Iacono et al. 2008)
Surface layer	Revised MM5 Monin-Obukhov scheme (Jiménez et al. 2012)
Surface model	Unified Noah Land Surface Model (Tewari et al. 2004)

844

845

Table 2. Summary of observations used in this study. The default observation error statistics provided in WRFDA system are used for assimilation in this study. The variables u, v, T, RH, Ps, and TPW denote zonal wind, meridional wind, temperature, relative humidity, surface pressure, and total precipitable water, respectively.

Observations	Descriptions	Variables	Observation errors (depending on vertical levels)
SOUND	Upper-air observation from radiosonde	u, v	1.1-3.3 m/s
		T	1 K
		RH	10-15%
PROFILER	Upper-air wind profile from wind profiler	u, v	2.2-3.2 m/s
PILOT	Upper-air wind profile from pilot balloon or radiosonde	u, v	2.2-3.2 m/s
AIREP	Upper-air wind and temperature from aircraft	u, v	3.6 m/s
		T	1 K
Scatwind	Scatterometer oceanic surface winds	u, v	2.5-3.8 m/s
SHIPS	Surface synoptic observation from ship	u, v	1.1 m/s
		T	2 K
		Ps	1.6 hPa
		RH	10%
SYNOP	Surface synoptic observation from land station	u, v	1.1 m/s
		T	2 K
		Ps	1 hPa
		RH	10%
BUOY	Surface synoptic observation from buoy	u, v	1.4-1.6 m/s
		T	2 K
		Ps	0.9-1 hPa
		RH	10%
GPSPW	Precipitable water vapor from global positioning system (GPS)	TPW	0.2 mm
METAR	Aviation routine weather report from automatic weather station (AWS)	u, v	1.1 m/s
		T	2 K
		Ps	1 hPa
		RH	10%
AMV	Conventional atmospheric motion vector data from geostationary satellite	u, v	2.5-4.5 m/s

853 Table 3. (Re)analyses and (re)forecasts and corresponding experiments used in this study.

Experiment	(Re)analysis	(Re)forecast
AdvHG (EARR)	Reanalysis from AdvHG	Generated using WRF
E3DVAR	Analysis from E3DVAR	Generated using WRF
WRF-based ERA5	Reanalysis from ERA5	Generated using WRF
WRF-based ERA-I	Reanalysis from ERA-I	Generated using WRF
ERA5_fromECMWF	Reanalysis from ERA5	Downloaded from ECMWF
ERA-I_fromECMWF	Reanalysis from ERA-I	Downloaded from ECMWF

854

855 Table 4. The 2×2 contingency table for dichotomous (yes-no) events.

Forecast	Observed		
	Yes	No	
Yes	Hits (A)	False alarms (B)	A + B
No	Misses (C)	Correct rejections (D)	C + D
	A + C	B + D	Total = A + B + C + D

856

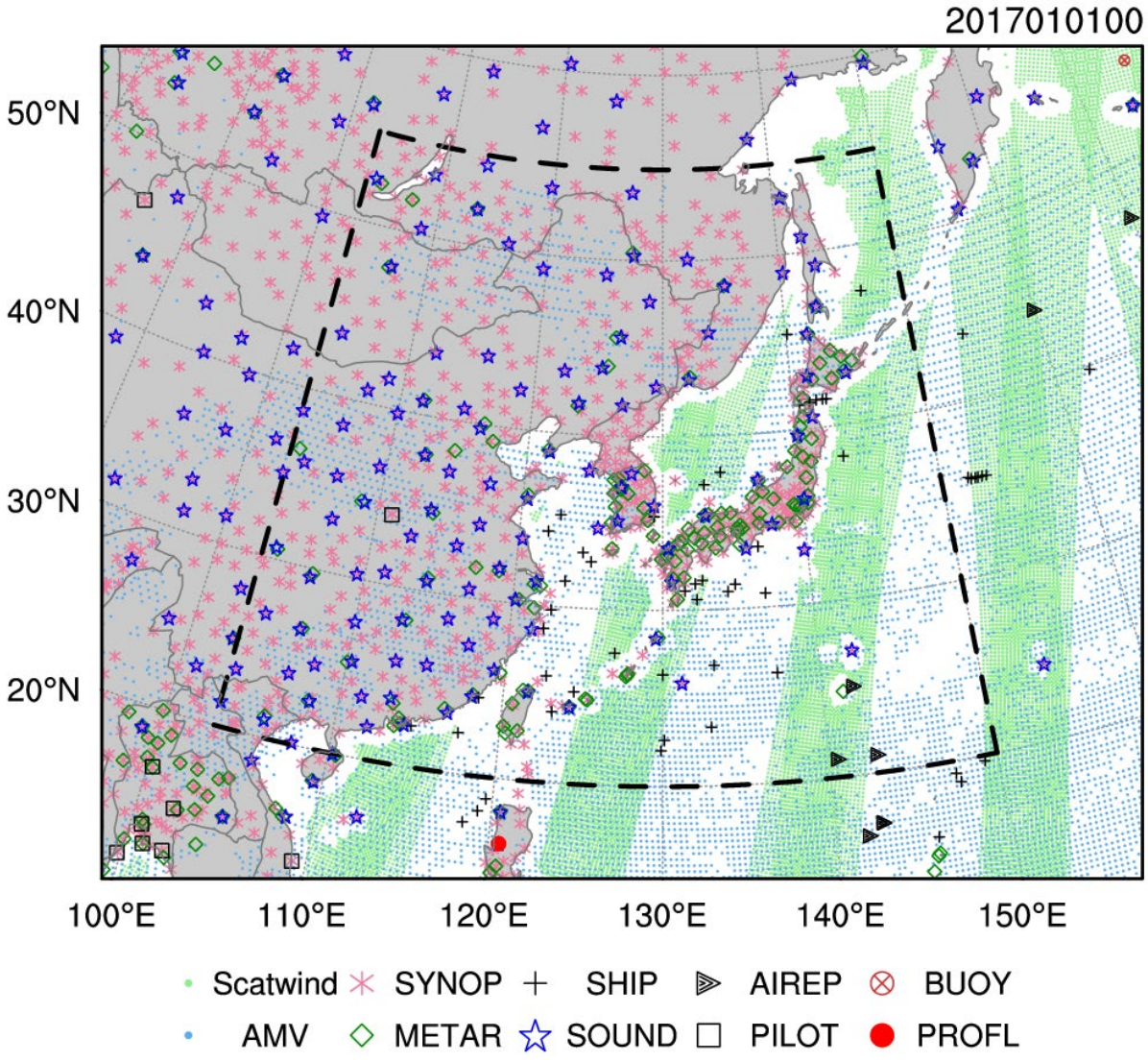

857

858 Figure 1. The East Asia Regional Reanalysis domain with different types of NCEP PrepBUFR
859 observations available for assimilation at 00 UTC on 1st of January in 2017. The black dashed
860 box denotes a verification area.

861

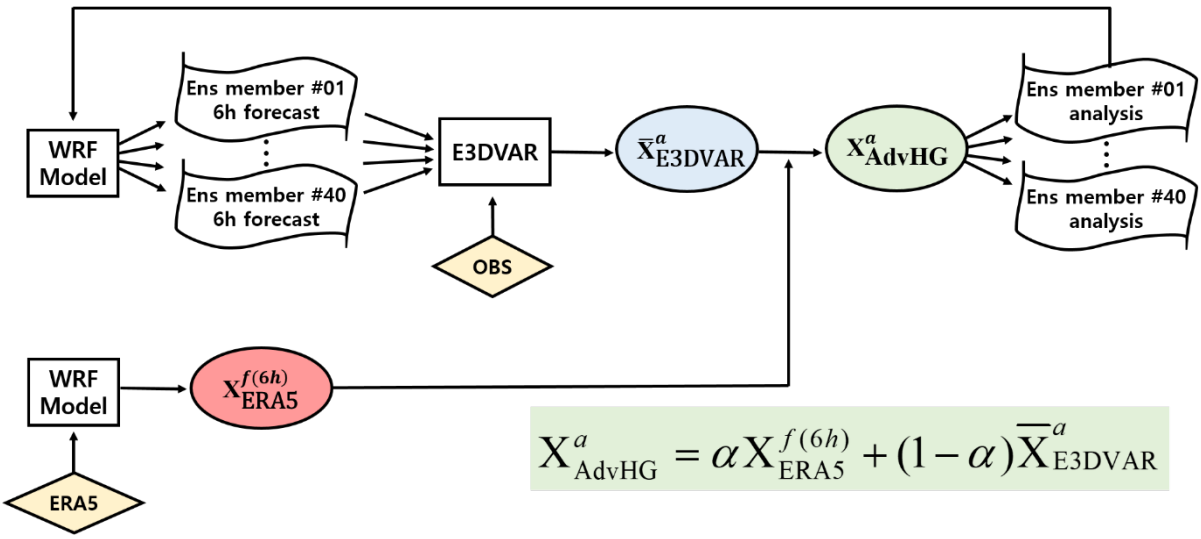

863 Figure 2. The schematic diagram of the advanced hybrid gain data assimilation method in the
864 East Asia regional reanalysis system.

865

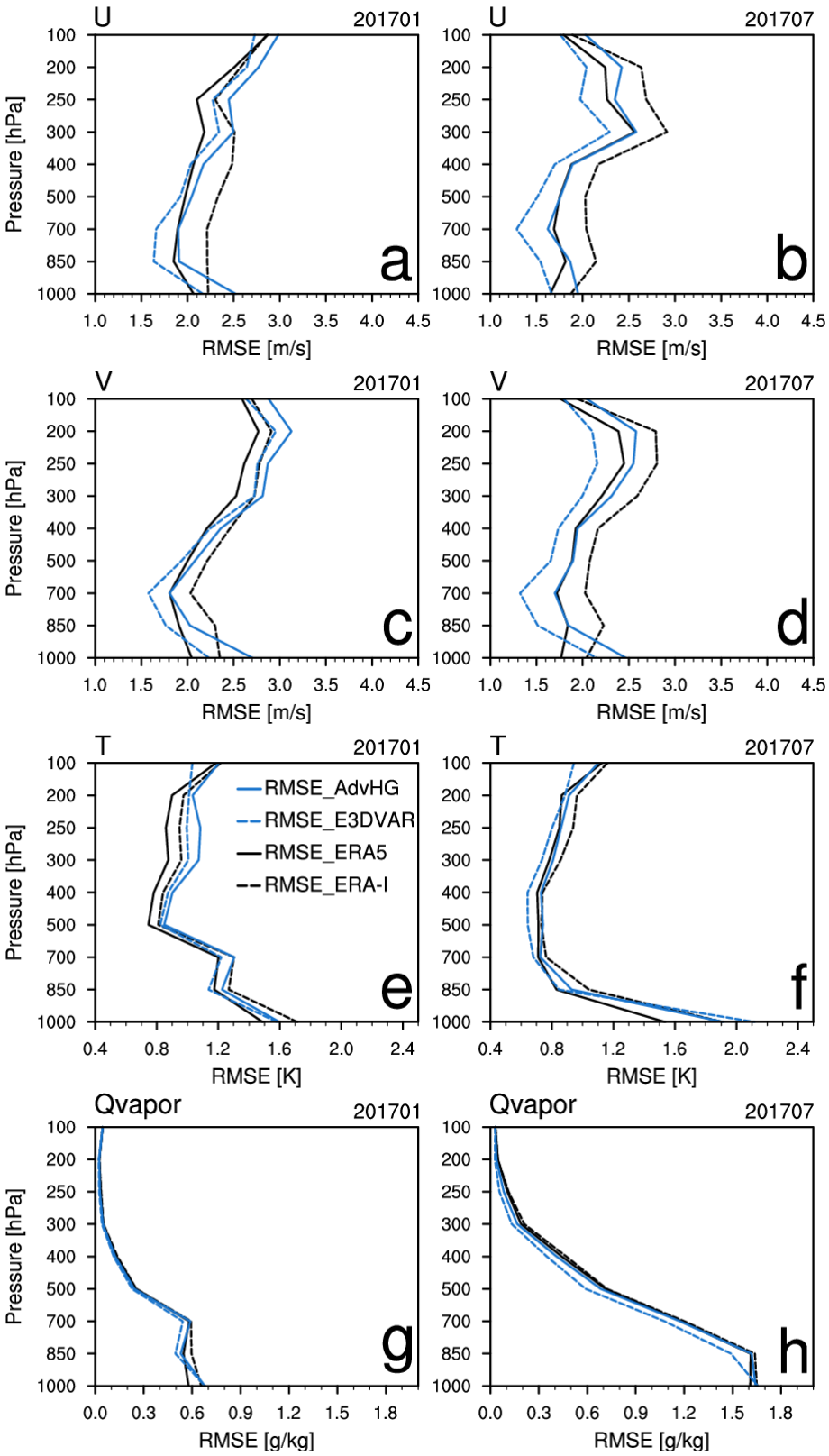

867 Figure 3. RMSEs of analysis of (a,b) zonal wind, (c,d) meridional wind, (e,f) temperature, and
868 (g,h) Qvapor (water vapor mixing ratio) from ERA-I (black dashed), ERA5 (black solid),
869 E3DVAR (blue dashed), AdvHG (blue solid) depending on pressure levels for (left) January
870 and (right) July in 2017.

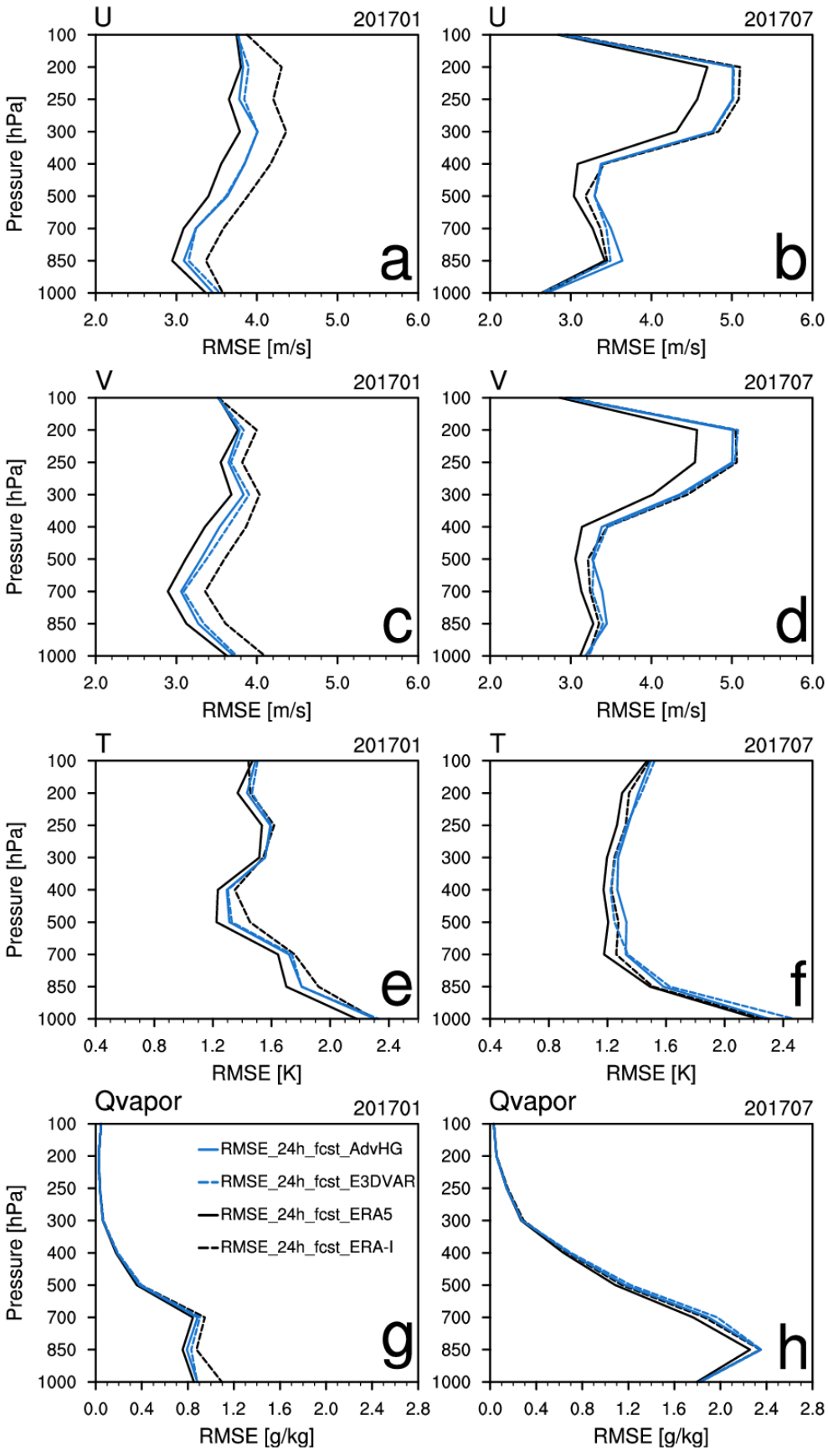

872 Figure 4. Same as Fig. 3 except for 24 h forecast.

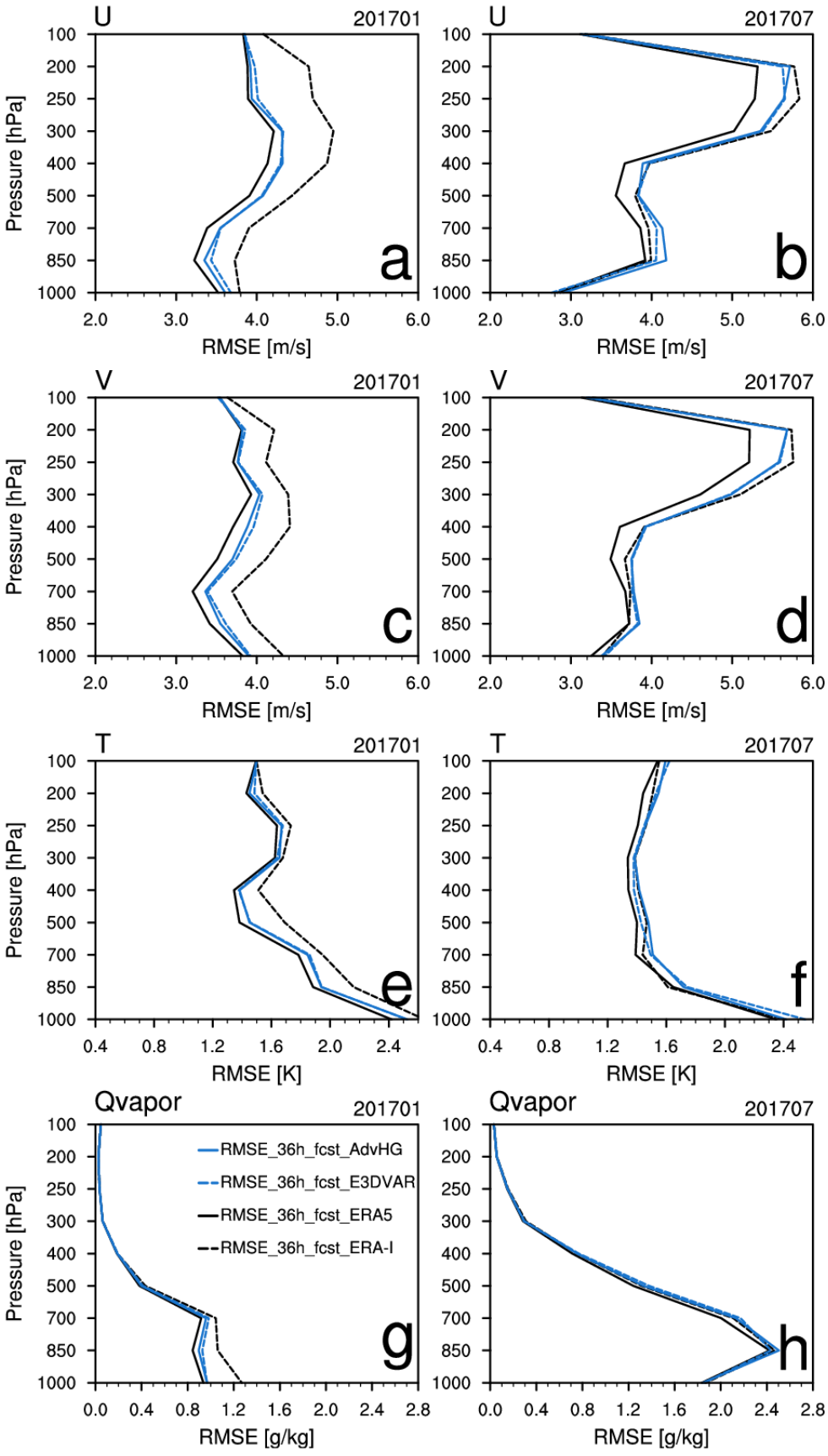

874 Figure 5. Same as Fig. 3 except for 36 h forecast.

875

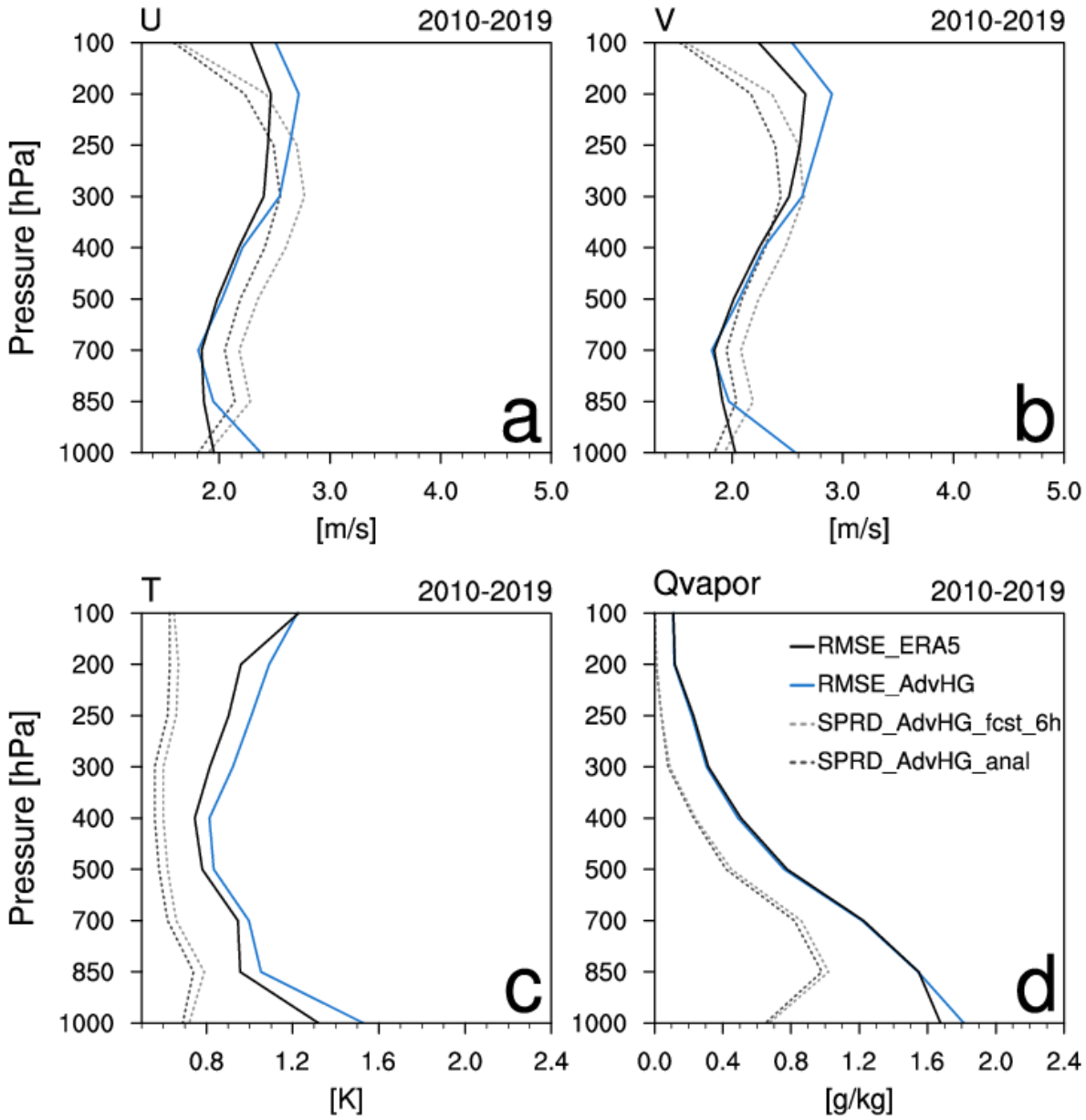

876

877 Figure 6. RMSEs of analysis of (a) zonal wind, (b) meridional wind, (c) temperature, and (d)
878 Qvapor (water vapor mixing ratio) from ERA5 (black solid) and AdvHG (blue solid) and
879 spreads of analysis (black dashed) and 6 h forecast (gray dashed) of AdvHG depending on
880 pressure levels averaged over the ten-year period of 2010–2019.

881

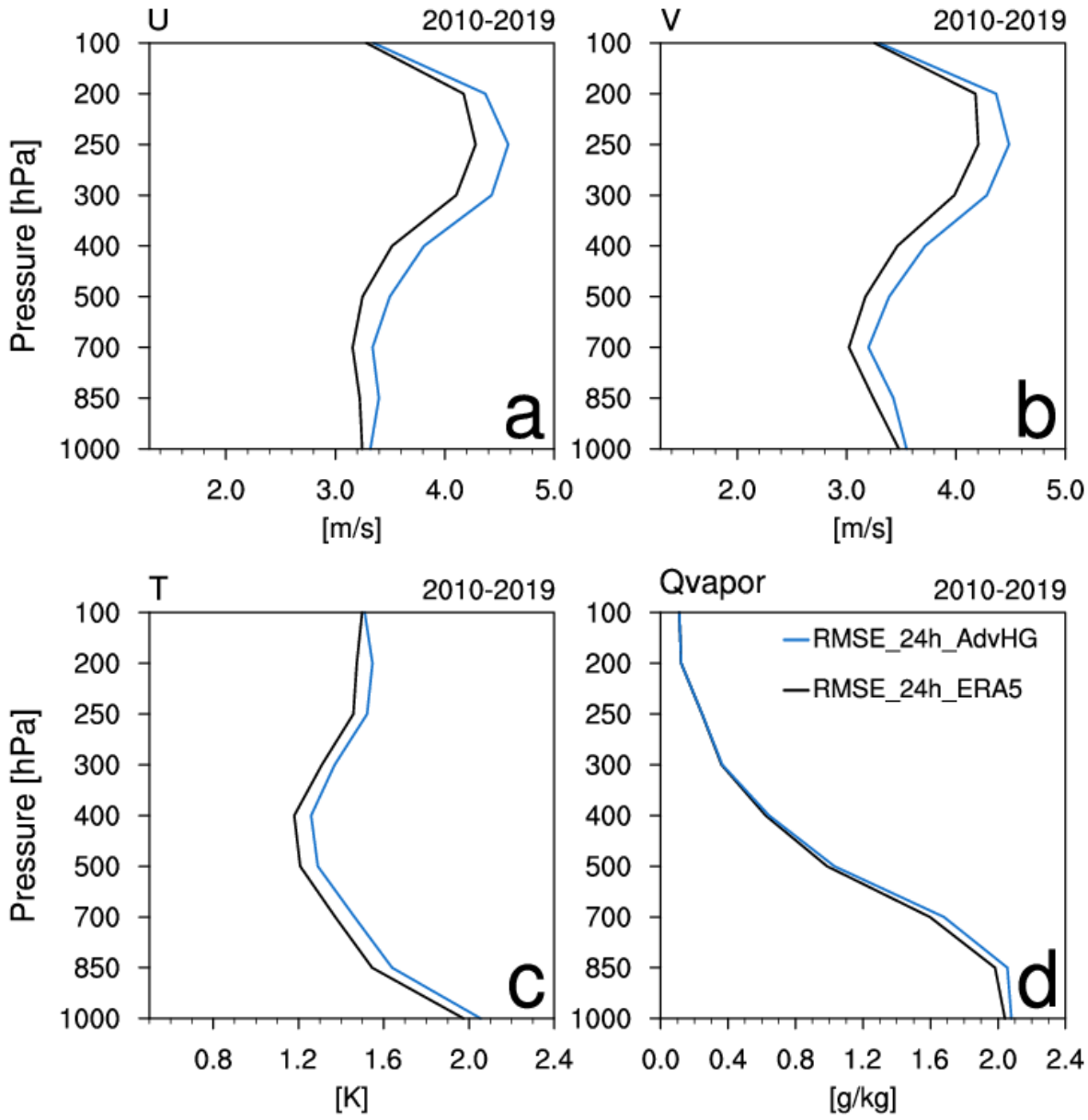

883 Figure 7. Same as Fig. 6 except for RMSE of 24 h forecast.

884

885

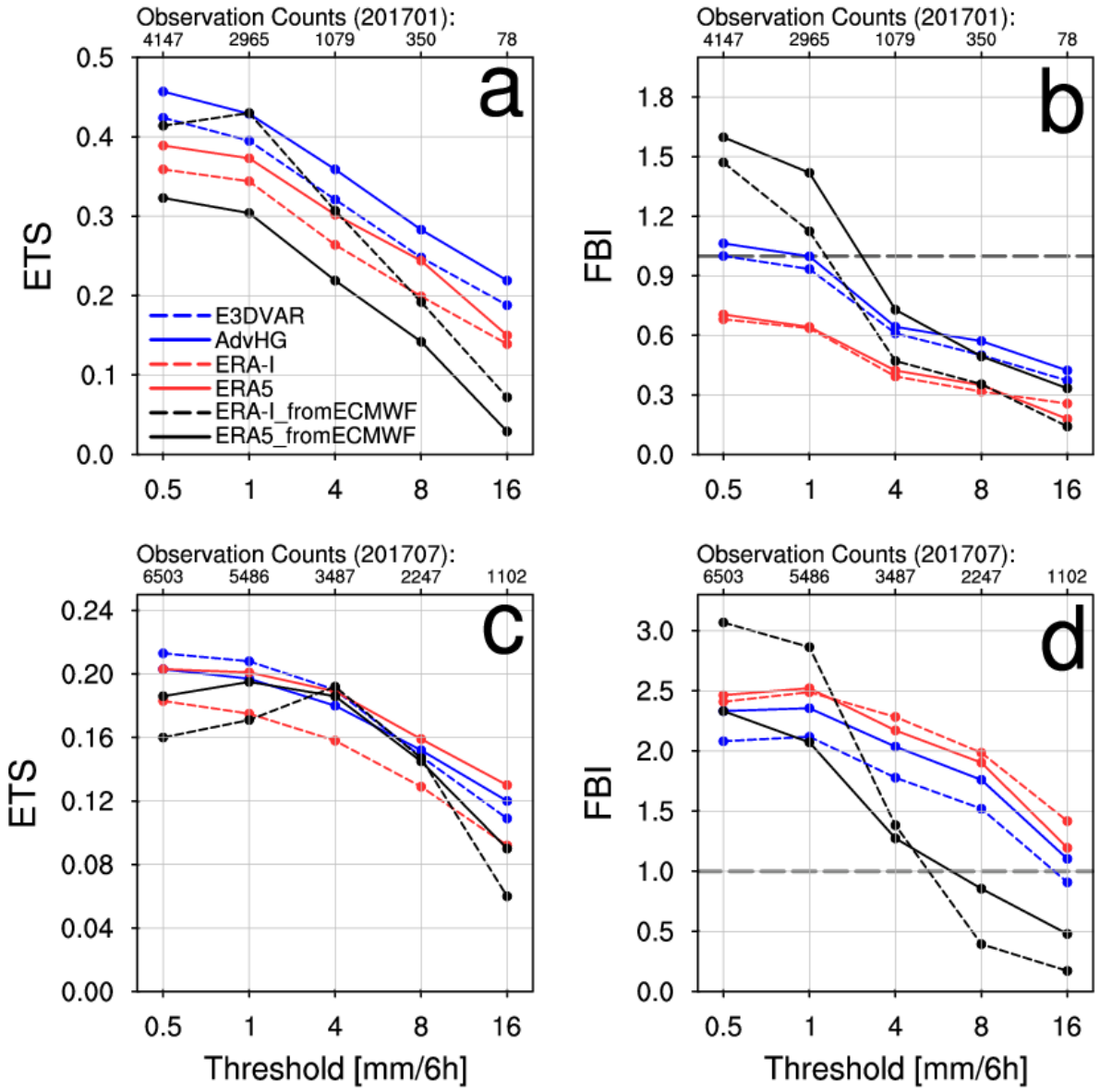

887 Figure 8. (a,c) ETS and (b,d) FBI for (a,b) January and (c,d) July in 2017 depending on
888 thresholds 0.5, 1, 4, 8, and 16 mm $(6\ h)^{-1}$.

889

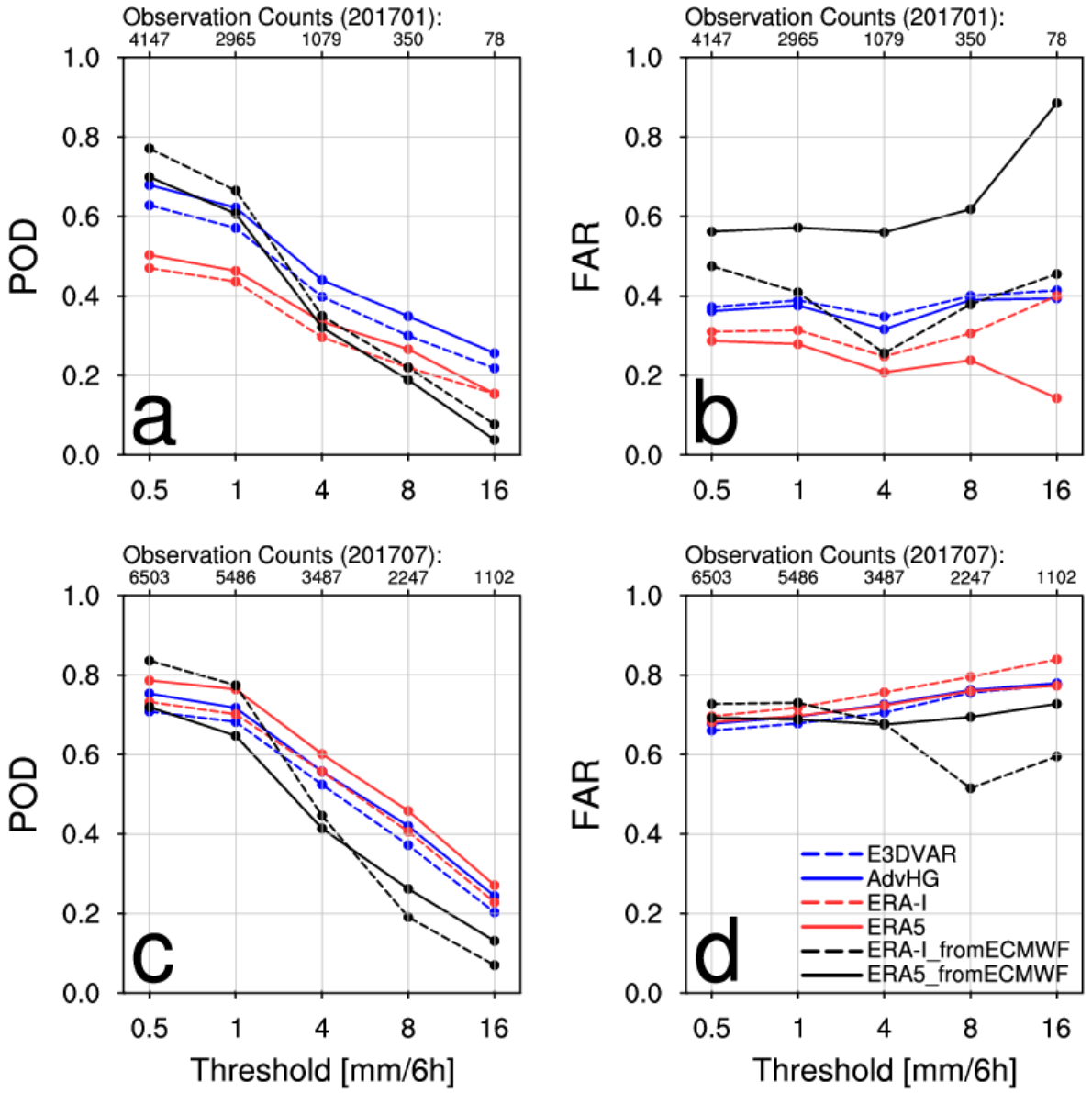

Figure 9. (a,c) POD and (b,d) FAR for (a,b) January and (c,d) July in 2017 depending on thresholds 0.5, 1, 4, 8, and 16 mm $(6\ h)^{-1}$.

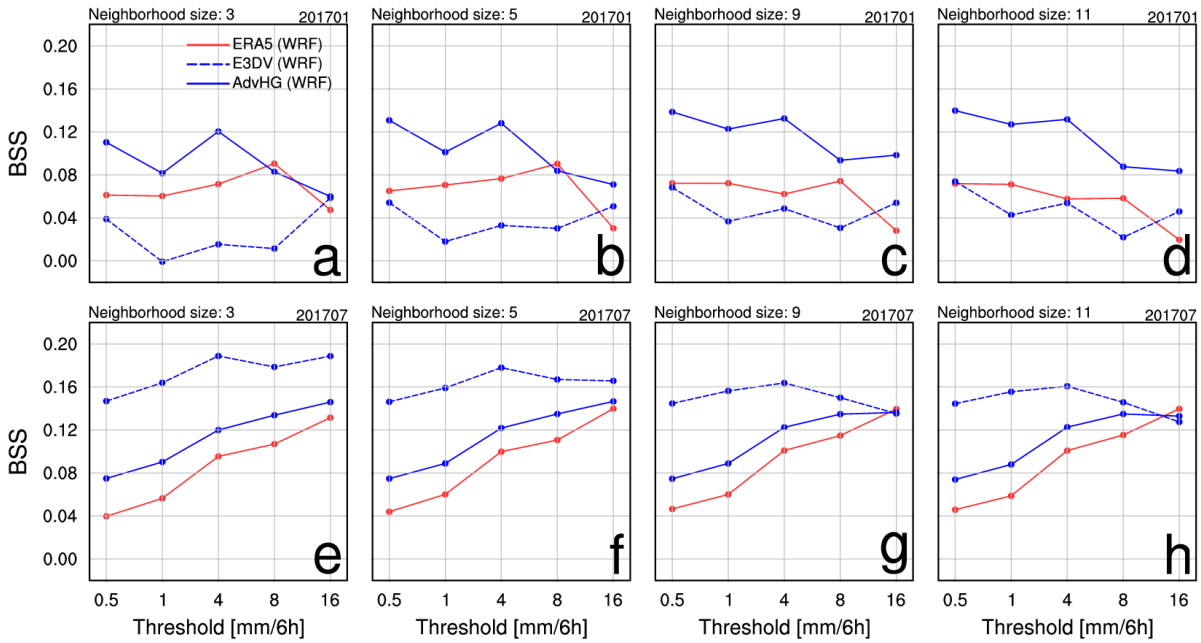

Figure 10. Brier skill score of the probabilistic postprocessed forecast with reference to the WRF-based ERA-I for (a-d) January and (e-h) July in 2017 (Blue solid: AdvHG, blue dashed: E3DVAR, red solid: WRF-based ERA5).

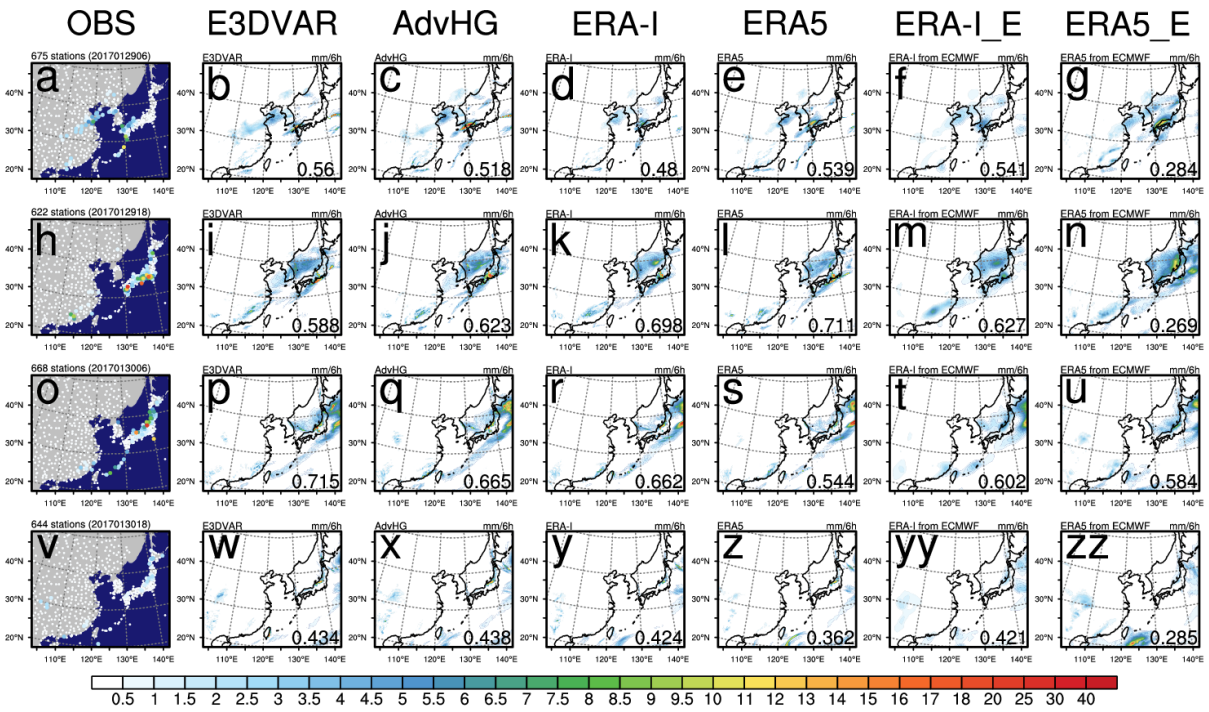

Figure 11. The spatial distribution of 6 h accumulated precipitation of (1st column) observation, (2nd column) E3DVAR, (3rd column) AdvHG, (4th column) ERA-I, (5th column) ERA5, (6th column) ERA-I_fromECMWF, and (7th column) ERA5_fromECMWF and the pattern correlation coefficient (PCC) shown at the bottom right of each figure at valid time (1st low, 3rd low) 06 UTC and (2nd low, 4th low) 18 UTC on 29th and 30th of January in 2017.

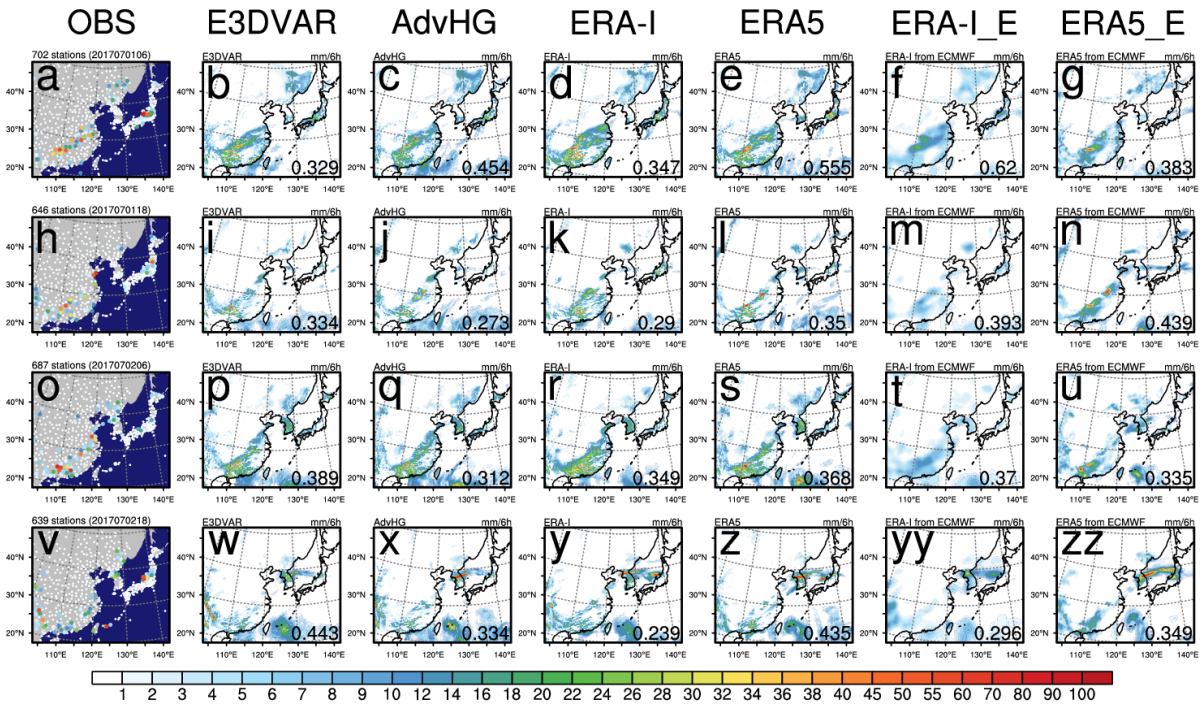

907 Figure 12. As in Fig. 11, but for 1st and 2nd of July in 2017.

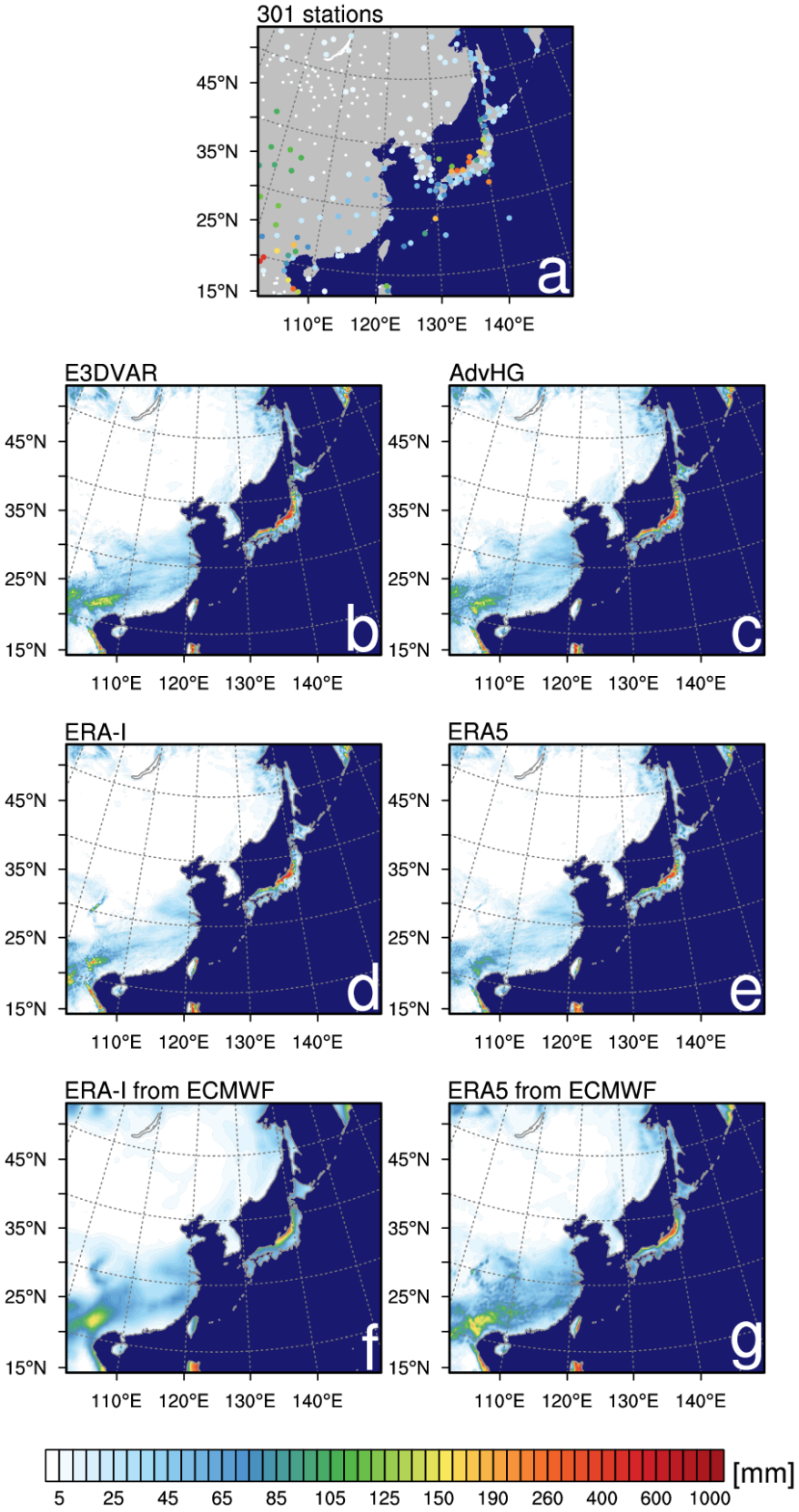

909 Figure 13. The spatial distribution of the monthly accumulated precipitation of (a) observations,
910 (b) E3DVAR, (c) AdvHG, (d) ERA-I, (e) ERA5, (f) ERA-I from ECMWF, and (g) ERA5 from
911 ECMWF for January 2017.

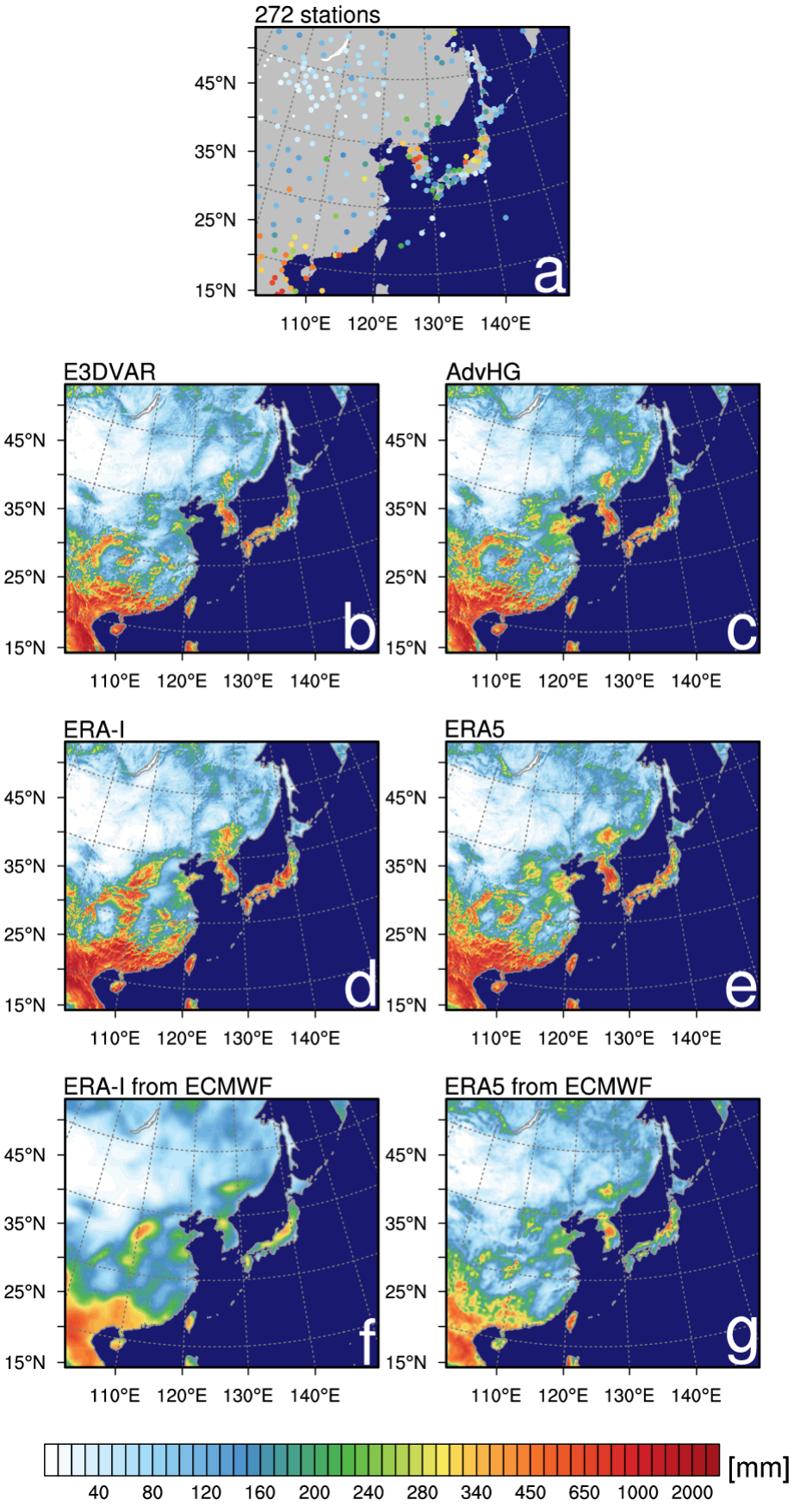

913 Figure 14. As in Fig. 13, but for July 2017.